# Interfacial engineering of a carbon nitride-graphene oxide-molecular Ni catalyst hybrid for enhanced photocatalytic activity

Hatice Kasap,[1] Robert Godin,[2] Chiara Jeay-Bizot,[2] Demetra S. Achilleos,[1] Xin Fang,[1] James R. Durrant,[2] Erwin Reisner[1,*]

[1]Department of Chemistry, University of Cambridge, Lensfield Road, Cambridge CB2 1EW, UK

[2]Department of Chemistry, Imperial College London, Exhibition Road, London SW7 2AZ, UK

Corresponding author:
reisner@ch.cam.ac.uk

## Abstract

Carbon nitrides ($CN_x$) are a promising class of photocatalyst for fuel and chemical synthesis as they are non-toxic and readily synthesized at a low cost. This study reports the enhanced photocatalytic activity for simultaneous alcohol oxidation and proton reduction when graphene oxide (GO) or reduced graphene oxide (RGO) is employed as an interlayer between a cyanamide-functionalized melon-type carbon nitride ($^{NCN}$**CN$_x$**) and a phosphonated Ni-bis(diphosphine) $H_2$-evolution catalyst (**NiP**). Introduction of the GO/RGO enhanced the activity three times, reaching a specific activity of 4655 ± 448 μmol $H_2$ (g $^{NCN}CN_x)^{-1}$ $h^{-1}$ with a **NiP**-based turnover frequency of 116 ± 3 $h^{-1}$. Mechanistic studies into this closed photo-redox system revealed that the rate of electron extraction from $^{NCN}$**CN$_x$** is rate limiting. GO/RGO is commonly employed to improve the electron transfer dynamics on nanosecond timescales, but time-resolved photoluminescence and transient absorption spectroscopy reveal that these properties are not significantly affected in our $^{NCN}$**CN$_x$-GO** hybrid on fast timescales (< 0.1 s). However, long lived “trapped-electrons” generated upon photoexcitation of $^{NCN}$**CN$_x$** in the presence of organic substrates are shown by photoinduced absorption spectroscopy to be quenched faster with GO/RGO, supporting that GO/RGO improves electron transfer from $^{NCN}$**CN$_x$** to **NiP** on timescales > 0.1 s. The absorption profile of **NiP** in the presence of different GO loadings reveals that GO acts as a conductive interfacial ‘binder’ between **NiP** and $^{NCN}$**CN$_x$**. The enhancement in activity therefore does not primarily arise from changes in the photophysics of the $^{NCN}$**CN$_x$**, but rather from GO/RGO enabling better electronic communication between $^{NCN}$**CN$_x$** and **NiP**.

**Keywords:** Photocatalysis, carbon nitride, graphene oxide, interface, charge transfer, spectroscopy

## Introduction

Solar-driven water splitting with semiconductor particles is a strategy to generate clean and renewable energy carriers.[1] In addition to harvesting a large portion of the solar spectrum, water-splitting systems also require efficient charge separation and delivery of multiple of such photogenerated charges to catalytic centers. Amongst common semiconductors, $TiO_2$ and ZnO are widely used due to their non-toxicity and stability.[2,3] However, the large bang gap of these metal oxides (3.2 eV) makes doping or sensitization with dyes, often expensive (ruthenium dyes) or unstable (organic dyes), essential to extend the absorption into the visible region.[4–6] Despite the small band gap associated with metal chalcogenide semiconductors such as CdSe, CdS and ZnSe quantum dots (1.73, 2.42 and 2.7 eV), they suffer from toxicity and/or photo-corrosion.[7–10] In order to develop sustainable photocatalytic systems, scientific focus is being shifted towards investigations on efficient, benign and scalable photocatalytic systems.[1] Carbon dots are emerging as a new class of metal-free, non-toxic and water-soluble alternatives to traditionally used photosensitisers, which are in principle scalable through bottom-up synthesis.[11–13] However, the lack of detailed structural understanding of these nanomaterials at a molecular level currently hampers the rational design to optimize photocatalytic activity.[14]

Polymeric carbon nitride, $CN_x$, has attracted great attention as a next generation photocatalyst due to its high stability, well positioned conduction (CB) and valence bands (VB) and composition based upon “earth-abundant” elements.[15–18] In the last decade $CN_x$ have been demonstrated to promote solar driven organic substrate oxidation,[19] pollutant degradation,[20,21] $H_2$ production,[22–24] and water splitting.[18,25,26] Yet their photocatalytic performance is typically limited by fast recombination of photogenerated hole−electron pairs. To overcome this limitation

many strategies have been proposed such as non-metal doping,[27–29] noble metal doping,[30–32] and nanoengineering of $CN_x$.[33,34] An alternative strategy is to design a system in which photogenerated holes or electrons are consumed faster than charge recombination reactions by accelerating charge transfer to the catalytic sites. Recently, we used a cyanamide surface-functionalized melon-type carbon nitride, $^{NCN}\mathbf{CN_x}$, in combination with a molecular nickel(II) bis(diphosphine) $H_2$-evolution catalyst, **NiP**, to simultaneously produce aldehyde and $H_2$ in 1:1 stoichiometry from alcohol oxidation and proton reduction, respectively.[35] This closed photocatalytic redox system displayed enhanced photoactivity compared to unfunctionalized (amino-terminated) carbon nitride, $^{H_2N}\mathbf{CN_x}$, which was attributed to the superior hole quenching ability of 4-methyl benzyl alcohol (4-MBA) in the presence of $^{NCN}\mathbf{CN_x}$. The slow transfer of the photogenerated electrons to the diffusional **NiP** was identified as the overall rate limiting step for this photocatalyst system.[35]

Interfacial engineering of semiconductors with charge separation layers can increase the lifetime of charge carriers and improve photocatalytic activity.[36] Graphene possesses high specific surface area (~ 2600 $m^2\ g^{-1}$), high mobility of charge carriers (~ 200 000 $cm^2\ V^{-1}\ s^{-1}$), and good chemical and electrochemical stabilities.[36–40] Moreover, graphene can be easily prepared from low-cost solution-based processes using graphite powder and it can be oxidized and exfoliated into graphene oxide (GO).[41–43] In order to balance the conductivity and hydrophilicity of GO, it is typical to convert it to reduced graphene oxide (RGO).[44,45] Many semiconductor−graphene composites have been studied and enhanced photocatalytic activities were reported in comparison to bare semiconductor towards $H_2$ production,[46–48] $CO_2$ reduction,[49–52] water splitting,[44,53–56] selective organic transformations,[57–60] and pollutant degradation.[61–64] This behavior was attributed to

the superior electron accepting and transfer capabilities of the GO derivatives, resulting in reduced charge recombination reactions and prolonged lifetimes for the photogenerated charge carriers in the semiconductors.[36,39,65] GO derivatives have also been utilized as efficient hole−extraction layer,[66–69] as well as an electron−extraction layers in heterojunction solar cells, due to their tunable work function and thin film formation ability.[70–72]

We have previously reported a noble metal free sacrificial photocatalytic system utilizing unfunctionalized $^{H_2N}$**CN$_x$** and molecular catalyst, **NiP**.[23] **NiP** is a hydrogenase-inspired molecular $H_2$-evolution catalyst,[73,74] which shows good activity in homogenous solution and when immobilized on semiconductor surfaces.[75–77] Subsequently we employed a more active, surface functionalized $^{NCN}$**CN$_x$** and replaced the sacrificial electron donor with a selective and almost quantitative alcohol oxidation reaction, coupled to **NiP** catalyzed proton reduction.[35] Here, we shed light on the improved photocatalytic performance of this $^{NCN}$**CN$_x$-NiP** photo-redox system in the presence of GO/RGO (Figure 1). The mechanism of the oxidation and reduction half reactions and the charge transfer between $^{NCN}$**CN$_x$**, GO/RGO and **NiP** are investigated. The $^{NCN}$**CN$_x$-GO-NiP** hybrid system is studied using optical spectroscopy techniques, namely time-resolved photoluminescence (tr-PL), transient absorption spectroscopy (TAS) and photoinduced absorption spectroscopy (PIAS), to understand the key kinetics leading to improved photocatalytic performance.

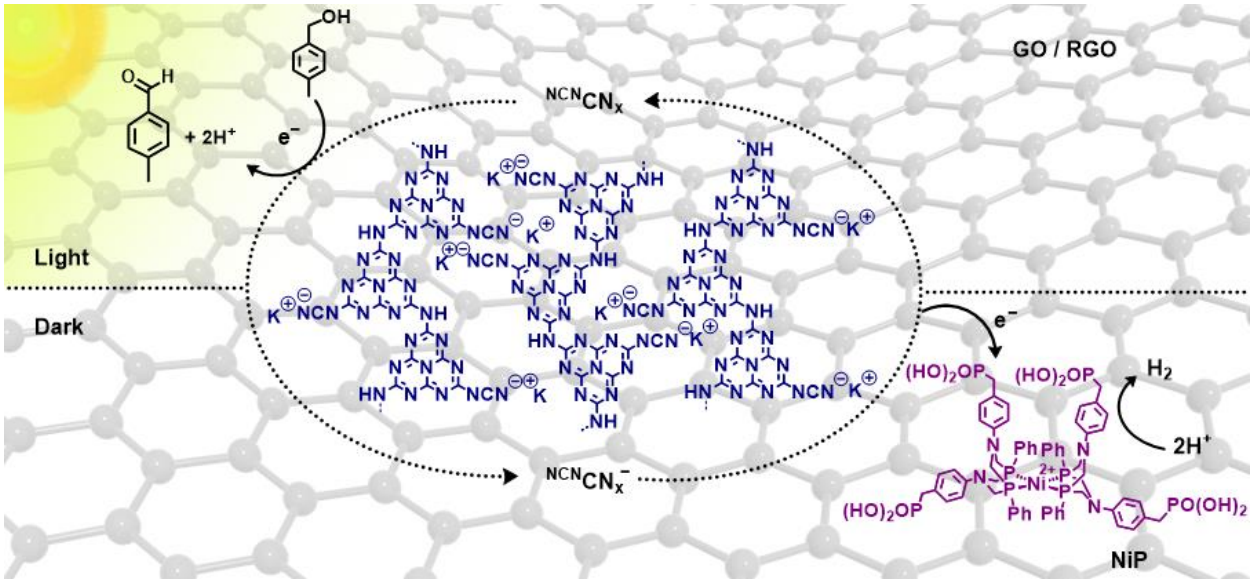


**Figure 1.** Schematic representation of photocatalytic **$^{NCN}CN_x$-GO-NiP** system. Irradiation of **$^{NCN}CN_x$** results in the formation of photoexcited state, which is quenched by 4-MBA and results in the formation of trapped electrons in **$^{NCN}CN_x$**. These 'ultra-long lived' electrons can then be transferred to **NiP** for proton reduction in the dark phase. The electronic communication between **$^{NCN}CN_x$** and **NiP** is enhanced by GO/RGO.

## Results and Discussion

**Assembly and Characterization of $^{NCN}CN_x$/GO system.** **$^{NCN}CN_x$**-GO/RGO hybrids were prepared by stirring **$^{NCN}CN_x$** (5 mg) and GO/RGO in aqueous solution (0.2 mg $mL^{-1}$) for 16 h prior to experiments. **$^{NCN}CN_x$**-$GO_x$/$RGO_x$ of different compositions were prepared [x denotes the content of GO and RGO in weight percentages loading in reference to **$^{NCN}CN_x$**; which ranges between 0.063 wt% (3.1 μg) and 50.00 wt% (2.5 mg)]. The samples were allowed to dry under atmospheric conditions, prior to characterization by Fourier transform infrared (FT-IR) and Raman spectroscopy, and the data of the hybrid were compared to bare **$^{NCN}CN_x$** and GO (Figure S1). The FT-IR

spectrum of bare $^{NCN}CN_x$ showed the characteristic heptazine core IR vibration at 803 $cm^{-1}$ and bridging secondary amine –C–N bending vibrations at 1307 and 1211 $cm^{-1}$, supporting the polymeric nature of the material. The appearance of the ν(C≡N) stretch at 2181 $cm^{-1}$ confirmed the presence of cyanamide groups on the surface of the material. The spectra recorded in the presence of either GO or RGO showed negligible differences compared the spectrum of bare $^{NCN}CN_x$ (Figure S1a).[24,78] The Raman spectrum of the bare GO showed the D and G bands at 1355 and 1597 $cm^{-1}$, respectively (Figure S1b).[79] The signals of the D and G bands are significantly suppressed in the hybrid $^{NCN}CN_x$-GO/RGO due to strong scattering of $^{NCN}CN_x$.

The X-ray diffraction (XRD) pattern of the **$^{NCN}CN_x$-GO** hybrid shows the characteristics bands observed for pure **$^{NCN}CN_x$,** indicating that the structure of the material is preserved after the physical mixing with GO (Figure S2).[24,78] More specifically, the hybrid shows the characteristic $^{NCN}CN_x$ peak at 28.2º, which corresponds to an interlayer spacing of 3.16 Å (002). In addition, the hybrid preserves that same (100) in-plane periodicity with pure $^{NCN}CN_x$, as indicated by the two bands at 9.83º (9.00 Å) and 8.04º (11.00 Å). The characteristic GO band at 10.9º (8.12 Å), due to (001) interlayer spacing, is less prominent in the XRD pattern of the hybrid due its low content.[24,80]

Scanning electron microscopy (SEM) images of **$^{NCN}CN_x$-GO** show that comparable morphological features as for bare $^{NCN}CN_x$ are observed (Figure S3). Transmission Electron Microscopy (TEM) images of **$^{NCN}CN_x$-GO** hybrids at different GO loadings show that GO sheets act as a scaffold to host the approximately 50 nm sized $^{NCN}CN_x$ particles (Figure S4). The UV-vis absorption profile of the **$^{NCN}CN_x$-GO** hybrid resembles the characteristic features of bare $^{NCN}CN_x$, $\lambda_{abs}$ < 450 nm, (Figure S5a). Photoluminescence (PL) studies were carried out to investigate changes in the

charge separation efficiency of $^{NCN}CN_x$ in the presence GO and RGO (Figure S5b). In contrast to literature reports,[38,39] we observe that introducing GO/RGO does not quench the emissive states in $^{NCN}CN_x$. This observation indicates that GO/RGO does not affect the rate of charge recombination under visible light irradiation in < 0.1 s timescale (see below for more details).[47,80]

**Assembly of Hybrid Photocatalyst and Activity. NiP** was synthesized and characterized as previously described.[75] $^{H_2N}CN_x$ and $^{NCN}CN_x$ were prepared from melamine by a slight modification of a published procedure (see experimental section for details).[23–25] $^{NCN}CN_x$ (5 mg) was added to an aqueous suspension of GO/RGO (0.2 mg $mL^{-1}$) in a photoreactor and stirred for 16 h prior to experiments. This was followed by the addition of an aqueous solution of **NiP** and ethylenediamine tetraacetic acid (EDTA) or potassium phosphate buffer ($KP_i$) with 4-MBA (30 µmol). The final suspension contained 3 mL of EDTA (0.1 M, pH 4.5) or $KP_i$ (0.1 M, pH 4.5). The photoreactors were sealed, purged with $N_2$ (containing 2% $CH_4$ as internal gas chromatography (GC) standard) and irradiated at 25 °C using a solar light simulator equipped with AM 1.5G filter, at 1 Sun intensity (100 mW $cm^{-2}$). The headspace $H_2$ gas was quantified periodically by GC, while oxidation products of 4-MBA were characterized in solution by $^1H$ nuclear magnetic resonance (NMR) spectroscopy.

The parameters of the system (solvent, amount of GO, size of GO, amount of $^{NCN}CN_x$) were systematically varied and optimized for $H_2$ production per catalyst, expressed as **NiP** turnover frequency ($TOF_{NiP,}$ mol $H_2$ (mol NiP)$^{-1}$ $h^{-1}$) and turnover number ($TON_{NiP,}$ mol $H_2$ (mol NiP)$^{-1}$) determined after 1 and 4 of irradiation respectively, as well as the conversion yield of alcohol after 4 h (Tables S1-S6).

The initial experiments were performed using EDTA (0.1 M) as a sacrificial electron donor (Figure 2a). Simulated solar light irradiation results in linear $H_2$ production during the first 4 h and a significant enhancement in photocatalytic activity was detected particularly in the presence of low GO loadings, < 0.50 wt% (25 μg), (Figure S6a). In the absence of GO, a $TOF_{NiP}$ of 38 ± 1 $h^{-1}$ was achieved, whereas the presence of $GO_{0.125}$ resulted in $TOF_{NiP}$ of 116 ± 3 $h^{-1}$. After 4 h of irradiation, three times higher $H_2$ production activity (17 ± 1 μmol, and $TON_{NiP}$, 348 ± 11) was recorded with $GO_{0.125}$ compared to that of bare $^{NCN}CN_x$. $^{NCN}CN_x$-$RGO_{0.125}$ has a comparable catalytic activity ($TOF_{NiP}$ of 102 ± 1 $h^{-1}$ and TON of 322 ± 6), potentially indicating *in situ* photoreduction of GO.[44]

It was previously reported that GO can itself act as a p- or n-type semiconductor, depending on the degree of its surface oxidation,[81] as well as photocatalyst for $H_2$ production.[82,83] Control experiments in the absence of $^{NCN}CN_x$ with GO/RGO-NiP only under simulated solar light and blue filtered ($\lambda$ > 495 nm) irradiation did not generate $H_2$, ruling out this possibility (Table S1). Increasing GO loadings above 0.50 wt% (25 μg) caused a substantial decrease in the activity (Figure S6a). This observation may be due to increased light scattering by GO, reducing the amount of light that can be absorbed by $^{NCN}CN_x$.[47]

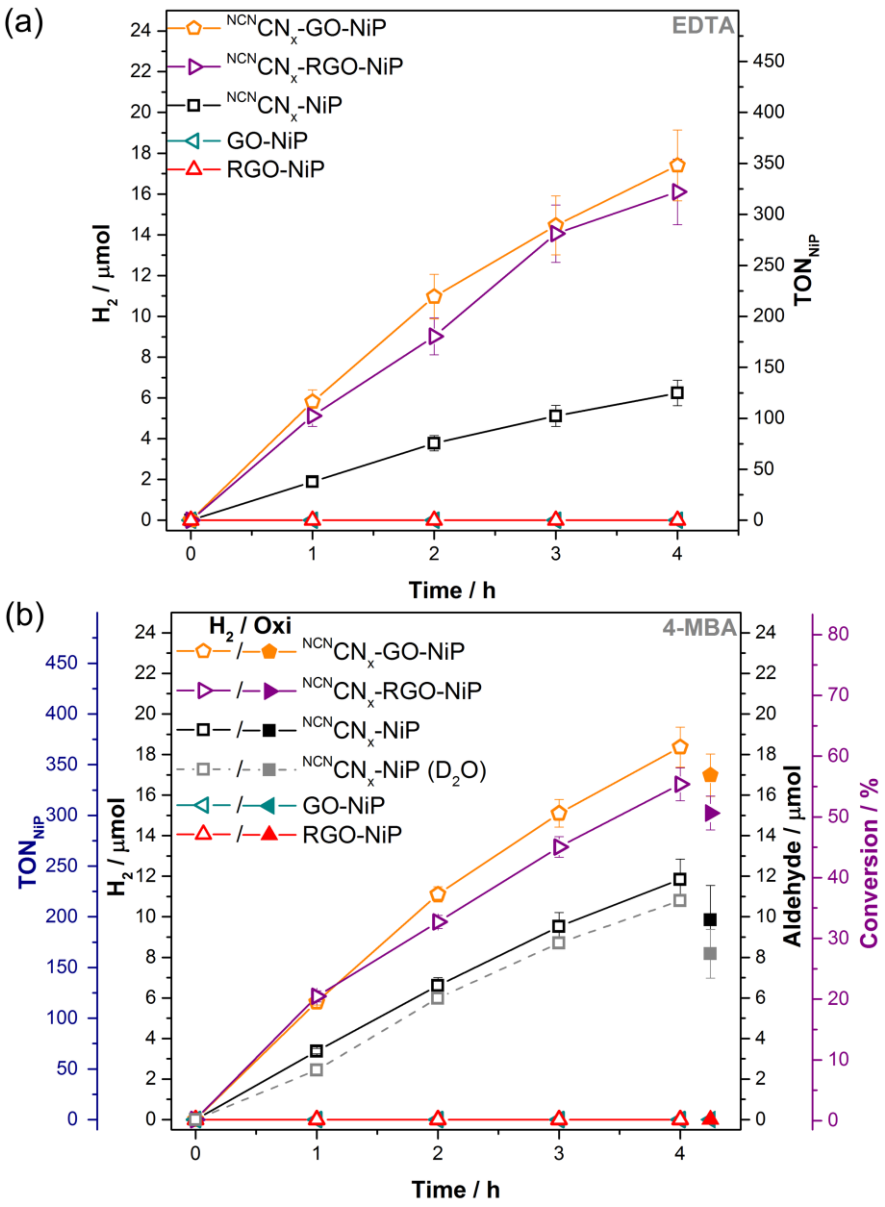


**Figure 2.** Photocatalytic $H_2$ production under simulated solar light irradiation (100 mW $cm^{-2}$, AM1.5G, 25 °C) with 5 mg of **$^{NCN}CN_x$**, **$^{NCN}CN_x$−GO** and **$^{NCN}CN_x$−RGO** (0.125 wt% loading of GO or RGO, 6.3 µg) in the presence of **NiP** (50 nmol) in (a) aqueous EDTA solution (0.1 M, pH 4.5, 3 mL), and (b) in aqueous $KP_i$ solution (0.1 M, pH 4.5, 3 mL) containing 4-MBA (30 µmol) under $N_2$. The experiment plotted as dashed gray trace was performed in deuterated water ($D_2O$). The pair of hollow and filled symbols of the same shape and color corresponds to $H_2$ and aldehyde production, respectively. The amount of aldehyde was quantified after 4 h of irradiation. Control experiments in the absence of **$^{NCN}CN_x$** and in the presence of RGO are also presented.

The enhanced photocatalytic performance of $^{NCN}$**CN$_x$** in the presence of GO/RGO encouraged us to replace excess EDTA by a closed redox system with stoichiometric and selective alcohol oxidation coupled to proton reduction (Figure 2b and S6b). In the presence of 4-MBA (30 µmol) with $^{NCN}$**CN$_x$** and $GO_{0.125}$, a specific activity of 1159 ± 29 µmol $H_2$ (g $^{NCN}CN_x)^{-1}$ $h^{-1}$ towards $H_2$ and aldehyde production, $TOF_{NiP}$ of 116 ± 3 $h^{-1}$ and $TON_{NiP}$ of 367 ± 20 were achieved, whereas bare $^{NCN}$**CN$_x$** showed a lower specific activity of 676 ± 27 µmol $H_2$ (g $^{NCN}CN_x)^{-1}$ $h^{-1}$, $TOF_{NiP}$ of 68 ± 3 $h^{-1}$ and $TON_{NiP}$ of 237 ± 20. Consistent with results recorded in EDTA solution, replacing $GO_{0.125}$ by $RGO_{0.125}$ in the presence of 4-MBA yielded similar activity with respect to the photocatalyst at 1216 ± 55 µmol $H_2$ (g $^{NCN}CN_x)^{-1}$ $h^{-1}$ and to the catalyst with $TOF_{NiP}$ of 122 ± 5 $h^{-1}$. The reaction rate for alcohol oxidation almost doubled in the presence of GO or RGO, reaching 17 µmol of selective 4-methyl benzyl aldehyde (4-MBAd) formation with a conversion yield of 57%. Bare $^{NCN}$**CN$_x$** reached 10 µmol 4-MBAd corresponding to 32% conversion under the same conditions. After 4 h of irradiation in the presence of GO/RGO approximately 18 µmol of $H_2$ and aldehyde were formed, corresponding to 50 % enhancement in photocatalytic activity in comparison to bare $^{NCN}$**CN$_x$**.

Control experiments with $^{NCN}$**CN$_x$-GO-NiP** in the absence of $^{NCN}$**CN$_x$** or **NiP** with 4-MBA in $KP_i$ buffer did not generate $H_2$ (Figure 2b). Aldehyde (4-MBAd) was also produced in the latter experiment due to ‘solar charging’ of the $^{NCN}$**CN$_x$** in the absence of catalyst (Table S7 and discussion below).[35]

The catalytic turnover rates and numbers of **NiP** are in broad agreement with previously reported $H_2$ production systems using colloidal light absorbers under sacrificial conditions. Solar light driven $H_2$ generation with **NiP** was first reported in the presence of phosphonated ruthenium tris(2,2’-bipyridine) (RuP) dye sensitized

$TiO_2$ in ascorbic acid (pH 4.5), which showed a $TOF_{NiP}$ of 72 ± 5 $h^{-1}$.[75] A hybrid system containing $^{H_2N}$**CN$_x$** and **NiP** in EDTA (pH 4.5) reported a $TOF_{NiP}$ of 109 ± 11 $h^{-1}$.[23] Sacrificial photo-$H_2$ generation was also demonstrated using amorphous and N-doped carbon-dots as light harvester with **NiP** in EDTA (pH 6), reaching $TOF_{NiP}$ of 41 $h^{-1}$ and $TOF_{NiP}$ of 143 $h^{-1}$ respectively.[11,12]

Tuning the amount of $^{NCN}$**CN$_x$** at high GO loadings resulted in excellent specific activity (Table S3, Figure S7). The highest specific activity of 4655 ± 448 µmol $H_2$ (g $^{NCN}CN_x)^{-1}$ $h^{-1}$ was achieved with 0.5 mg of $^{NCN}$**CN$_x$** in the presence of 50 wt% GO loading (0.25 mg) and 50 nmol **NiP**. The $H_2$ production rate is amongst the highest reported in the literature with respect to mass of carbon nitride and the highest for selective organic oxidation coupled to fuel generation.[84–88] Previously reported semiconductor-graphene heterojunction systems have been studied with a sacrificial electron donor and noble metal proton reduction catalysts (Table S8).[89] For $CN_x$ systems, only a Eosin Y (EY) sensitized $CN_x$-GO composite with a Pt catalyst in a sacrificial triethanolamine (TEOA) solution shows comparable activity to the system developed in this work (3820 µmol $H_2$ (g $^{NCN}CN_x)^{-1}$ $h^{-1}$).[90] The high activity of our $^{NCN}$**CN$_x$-GO-NiP** hybrid is even comparable to a toxic CdS/graphene composite with Pt, which reaches up to 6000 µmol $H_2$ (g $^{NCN}CN_x)^{-1}$ $h^{-1}$.[91,92] $^{NCN}$**CN$_x$-GO-NiP** therefore demonstrates benchmark photoactivity for a precious metal free, single photo-absorber system. In addition, the system does not rely on excess sacrificial electron donor and converts an organic substrate cleanly into a value-added product in high yield.

Different sizes of GO sheets, <1−5 µm, were also studied to improve the understanding of the interaction between $^{NCN}$**CN$_x$** and GO, but only marginal variations in photocatalytic performance were observed (Figure S8).

The photocatalytic behavior of melon-type, amine terminated **$^{H_2N}CN_x$** was also studied in EDTA and $KP_i$ containing 4-MBA (Figure S9 and S10). As for **$^{NCN}CN_x$**, introduction of GO and RGO enhanced the photocatalytic activity by at least 50 %, demonstrating the more general ability of GO and RGO to improve the performance for carbon nitride photocatalysts.

**Light-dark charging cycle of $^{NCN}CN_x$.** We have previously established that light exposure of a yellow suspension of **$^{NCN}CN_x$** in the presence of an organic substrate results in the formation of blue **$^{NCN}CN_x$**.[35] This blue state is associated with ultra-long lived “trapped electrons” accumulated in **$^{NCN}CN_x$** with lifetimes on the order of hours. Addition of a catalyst such as **NiP** can release these low potential electrons in a dark phase to produce $H_2$. This unique behavior therefore allows decoupling of oxidative and reductive half-reactions temporarily, making it possible to generate a solar fuel in the dark.[35,93] Thus, the electron storage capacity of **$^{NCN}CN_x$-GO** (5 mg) hybrid suspensions in an aqueous $KP_i$ solution with 4-MBA (30 µmol) without **NiP** were studied. The anaerobic suspensions were irradiated for 30 min, 2 and 4 h and then moved into the dark (Figure 3). The $H_2$ evolution performance was monitored after injecting **NiP** (50 nmol in KPi solution) to the pre-irradiated, blue suspensions using an airtight syringe (Table S7).

Independently of the length of charging interval, discharging rates of approximately 0.40 mmol $e^-$ (g $^{NCN}CN_x)^{-1}$ $h^{-1}$ were observed, based on 1 µmol of $H_2$ being produced from 2 µmol of radicals, per 5 mg of **$^{NCN}CN_x$** after one hour of **NiP** injection in the dark. Short-term irradiation resulted in rapid discharge upon injection of **NiP**, whereas 4 h light-exposure required a longer time to consume the larger number of trapped electrons. The total amount of trapped electrons and

corresponding dark $H_2$ evolution saturated after 4 h irradiation and irradiating the samples for 12 h did not increase the number of accumulated charges (Table S7).

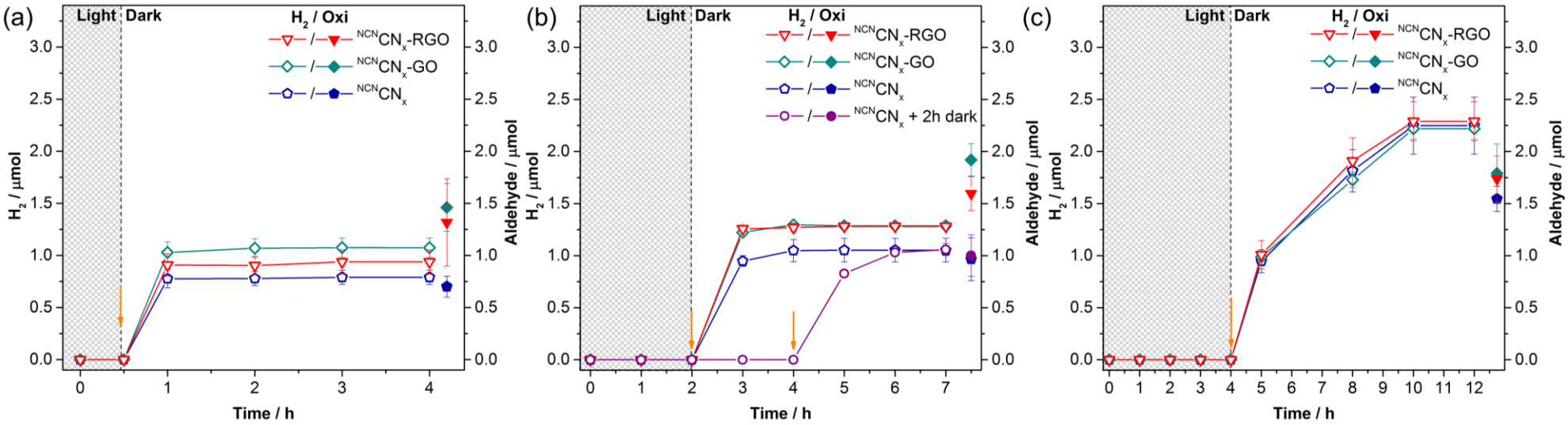


**Figure 3.** Photocatalytic suspensions were prepared with 5 mg of $^{NCN}CN_x$, $^{NCN}CN_x$**−GO** and $^{NCN}CN_x$**−RGO** (0.125 wt% loading of GO or RGO, 6.3 μg) in aqueous $KP_i$ solution (0.1 M, pH 4.5, 3 mL) containing 4-MBA (30 μmol) without **NiP** under $N_2$. The samples were irradiated for (a) 30 min, (b) 2 h and (c) 4 h under 1 sun simulated solar light irradiation (100 mW $cm^{-2}$, AM1.5G) at 25 °C. The suspensions were then moved into the dark and an anaerobic **NiP** solution (50 nmol in $KP_i$ solution) was injected. The pair of hollow and filled symbols of the same shape and color corresponds to $H_2$ and 4-MBAd production, respectively. The amount of aldehyde formed is detected after 30 min, 2 and 4 h of irradiation in (a), (b) and (c), respectively. The orange arrows indicate the point of **NiP** injection; a control experiment with the vial kept in dark for 2 h before injection of **NiP** is shown in (b).

The amount of $H_2$ detected provides an indirect measure on the total number of heptazine based radicals generated during irradiation of the material (Table S9).[93] After 30 min of irradiation, 0.8 ± 0.1 µmol of $H_2$ was generated with bare $^{NCN}\mathbf{CN_x}$, whereas $^{NCN}\mathbf{CN_x}$-GO or RGO hybrids produced 1.1 ± 0.1 and 0.9 ± 0.1 µmol, respectively (Figure 3a). Assuming that trapped electrons are quantitatively converted into $H_2$, we can estimate that 2.1 ± 0.2 and 1.9 ± 0.2 µmol of radicals are accumulated in the $^{NCN}\mathbf{CN_x}$-GO and RGO hybrids, respectively (1.6 ± 0.1 µmol for bare $^{NCN}\mathbf{CN_x}$). This corresponds to approximately a 1:10 ratio of radical to heptazine units in $^{NCN}\mathbf{CN_x}$. After 4 h of irradiation a saturation concentration of trapped electrons was reached and approximately 2.25 µmol $H_2$ was detected, which corresponds to 4.50 ± 0.37 µmol of radicals (Figure 3c) or roughly a 1:5 ratio of radicals to heptazine units.

**Mechanisms of Oxidation and Reduction.** Mechanistic studies on organic substrate oxidation with colloidal light harvesters such as $CN_x$,[19,94,95] $TiO_2$,[96–98] and $BiVO_4$ [99,100] are common, but only a few reports exist on high-yielding alcohol photo-oxidation under $N_2$, which precludes the formation and potential involvement of reactive oxygen species.[101–103] To gain mechanistic insights (in particular for hole transfer from $CN_x$ to 4-MBA) we avoided the use GO and RGO in the photocatalytic suspension (see also time-resolved kinetics study below).

To identify the source of protons for $H_2$ production, $KP_i$ buffer was prepared in $H_2O$ and $D_2O$ (Figure 2b, Figure S11a and Table S10). The headspace gas produced was monitored by GC and characterized by mass spectrometry (MS), through examining the composition of the gases with mass/charge ratios between 1 and 5 amu over the irradiation period of 4 h (Figure S11a, inset). Over the course of

4 h, linear gas production at a comparable rate was observed regardless of using $H_2O$ or $D_2O$ as solvent. In the presence of $D_2O$, the peak corresponding for $D_2$ grew selectively over time with negligible amounts of $H_2$ and HD being detected. This indicated that aqueous protons were selectively delivered to **NiP** for $H_2$ formation. The rate of $H_2$ gas production was not affected by $D_2O$ substitution, indicating that O−H/D bond breaking is not a rate-determining step for proton reduction.[104]

The kinetic isotope effect (KIE) of an isotopically labeled 4-MBA substrate was then studied by using α-$D_2$ benzyl alcohol (BA). The substitution with $D_2$-BA did not influence the rate of proton reduction and MS analysis confirmed that the headspace gas was $H_2$ (Figure S11b), demonstrating that aliphatic protons from BA were not used for proton reduction. Independent of BA labeling, around 6 µmol of aldehyde is being produced after 4 h of irradiation, showing that the rate of proton abstraction from BA is not limiting the oxidation process. The first and rate-limiting step of oxidation is presumably hole transfer from photoexcited $^{NCN}\mathbf{CN_x}$ to the substrate (Figure S11c).[105,106]

Alcohol oxidation was further investigated by under a $N_2$ or air atmosphere without NiP (Figure S12). After 4 h of irradiation, selective production of 2 and 14 µmol of 4-MBAd was detected under $N_2$ and air atmospheres, respectively (for comparison, 10 µmol 4-MBAd are detected in the presence of **NiP** and $N_2$). These results indicate that the presence of a strong electron acceptor such as $O_2$ assists faster abstraction of photo-generated electrons from $^{NCN}\mathbf{CN_x}$, quickly regenerating the ground-state photocatalyst and increasing the turnover frequency for alcohol oxidation.[96,98]

The possibility of hydroxyl radical ($HO^{\bullet}$) formation was explored by using the hydroxyl radical scavenger benzene-1,4-dicarboxylic acid (terephthalic acid, THA).[107]

Hydroxylation of THA by $HO^{\bullet}$ yields a highly fluorescent THA-OH, with an emission at 426 nm when excited with 315 nm light.[107] $^{NCN}$**CN$_x$** suspensions irradiated in the presence of THA for one hour showed an insignificant amount (< 0.02 μmol) of THA-OH formation (Figure S13), indicating that this is a minor reaction pathway for the oxidation reaction. This is supported by the mismatch between the valence band position of $^{NCN}$**CN$_x$** (approximately 1.4 V *vs* the normal hydrogen electrode (NHE) at pH 7), and the redox potential of $^{-}OH$ to hydroxyl radicals ($E°(HO^{\bullet}/HO^{-})$ = 2.4 V *vs* NHE).[19,108] Photocatalytic substrate oxidation under $O_2$ atmosphere is believed to occur through superoxide radical formation, $O_2^{\bullet-}$, however this possibility can be excluded in the reported system as the experiments are carried out under $N_2$.[19]

Our mechanistic studies therefore support that presumably direct hole transfer occurs first from photoexcited $^{NCN}$**CN$_x$** to 4-MBA, followed by slow electron transfer from $^{NCN}$**CN$_x$** to **NiP** to reduce aqueous protons to $H_2$ (Figure S11c).[109] Consumption of the photogenerated charge carriers is ultimately essential to promote the production of $H_2$ and aldehyde in 1:1 stoichiometry and close the photo-redox cycle, but the oxidative and reductive half-reactions can be temporarily, and in principle, spatially decoupled.[102]

**Time-resolved spectroscopy.** Previously reported TAS measurements indicated that 4-MBA quenches the photogenerated holes on $^{NCN}$**CN$_x$** on timescale faster than 3 μs, while the extraction of the photoexcited electrons by **NiP** takes longer than 2 s.[35] In agreement with the mechanistic studies above, the photo-system is limited by hole transfer to 4-MBA and the accumulation of the low potential electrons in the $^{NCN}$**CN$_x$** on the short timescale, whereas on the longer timescale it is limited by the rate of electron extraction from 'electron-saturated' $^{NCN}$**CN$_x$** (Figure 1). Acceleration of the rate of electron extraction from $^{NCN}$**CN$_x$** would decrease the steady-state

concentration of trapped electrons in $^{NCN}$**CN$_x$** and reduce charge recombination losses. In turn, this will allow an overall higher conversion of 4-MBA and higher yield of electron transfer to **NiP**. We investigate here whether this is the case when the graphene based conductive scaffolds GO and RGO are introduced in the photocatalytic system.[110]

We studied the improved photocatalytic activity of $^{NCN}$**CN$_x$** in the presence of GO and RGO first using time-resolved photoluminescence spectroscopy (tr-PL), namely time correlated single photon counting (TCSPC) to record the fast PL decay process. For the TCSPC experiments samples were excited at $\lambda_{ex}$ = 404 nm and decay of the emissive states was monitored at $\lambda_{em}$ = 490 nm under Ar atmosphere. Both bare $^{NCN}$**CN$_x$** and $^{NCN}$**CN$_x$**-GO/RGO hybrids showed similar decay profiles in the absence and presence of 4-MBA (Figures S14 and S15). These results indicate that the interface between $^{NCN}$**CN$_x$** and GO/RGO does not improve the charge separation of the monitored emissive states on the ns timescale. This is a surprising observation in comparison to previously reported semiconductor-graphene hybrid/composite systems, where quenching of PL is a characteristic behavior, due to faster charge separation of the emissive excitonic states.[38,39]

Transient absorption spectroscopy (TAS) was subsequently performed to follow the charge transfer reactions in $^{NCN}$**CN$_x$** and GO/RGO hybrids on µs-s timescales. In contrast to tr-PL, TAS measurements monitor both emissive and non-emissive states generated in the material after photoexcitation. Photoexcitation ($\lambda_{ex}$ = 355 nm) of $^{NCN}$**CN$_x$** produced a broad photoinduced absorption signal in the 470−1000 nm range (Figure S16a). Similar to behavior observed in metal oxides, the decay of the signal in $^{NCN}$**CN$_x$** follows a power law and is attributed to bimolecular electron-hole recombination (Figure S16b). The exponent of the power law is smaller

than unity (~ 0.43), suggesting that a trapping/detrapping process plays a significant role in excited state dynamics of $^{NCN}\mathbf{CN_x}$, consistent with relatively slow time scale for the recombination process.[111,112]

Typical μs-TAS decays for $^{NCN}\mathbf{CN_x}$ suspension with and without 4-MBA under Ar were also recorded (Figure S17) at $\lambda_{ex}$ = 355 nm pulsed laser excitation with monitoring at 610 nm. In the absence of 4-MBA a decreasing decay is observed in the absorption profile until it remains nearly constant with a low amplitude at 1 ms after the light impulse. In the presence of 4-MBA a constant absorbance is reached from 1 μs with no decay over time (note that data > 100 ms is affected by $^{NCN}\mathbf{CN_x}$ settling, see below). In line with previous observations, this persistent signal is assigned to long-lived trapped electrons in $^{NCN}\mathbf{CN_x}$.[35,93]

To gain knowledge on how the interface between $^{NCN}\mathbf{CN_x}$ and GO or RGO are affecting the photophysics of $^{NCN}\mathbf{CN_x}$ on the μs-s timescale, TAS decays were recorded both in the absence and presence of 4-MBA with bare $^{NCN}\mathbf{CN_x}$ and hybrid systems containing various GO/RGO loadings (Figure 4). The results show that charge recombination took place faster than 1 ms in the absence of 4-MBA, with similar decay profiles with or without GO/RGO (Figure 4a). In the presence of 4-MBA (Figure 4b), a constant absorbance is reached within the time resolution of the setup and indicated that the photogenerated holes are quenched faster than 1 μs. In all cases, the transient absorption traces recorded for bare $^{NCN}\mathbf{CN_x}$ and GO or RGO hybrid systems showed no significant differences. In addition to comparable signal amplitudes, we also note that the decay kinetics are unaffected by the presence of GO or RGO (Figure S18), inconsistent with charge separation across the $CN_x$/GO interface. The results support our interpretation of the PL and tr-PL data, ruling out the possibility of GO and RGO influencing the charge carrier dynamics of $^{NCN}\mathbf{CN_x}$ by

enhancing the separation of photogenerated charges on shorter than s timescale.[47,113,114] In line with this observation, TAS experiments conducted for $^{H_2N}\mathbf{CN_x}$ also showed no difference between bare $^{H_2N}\mathbf{CN_x}$ and GO/RGO hybrids (Figure S19). The slightly lower signal amplitude for bare $^{H_2N}\mathbf{CN_x}$ in the absence of 4-MBA or **NiP** (Figure S19a) is attributed to experimental fluctuations and is in line with differences up to 20% observed in repeated measurements (Figure S20). Importantly, no changes in the decay kinetics are again observed (Figure S21). The difference between the activity of $^{NCN}\mathbf{CN_x}$ in the presence of 4-MBA and EDTA (Figure 2) were investigated by monitoring the µs-TAS decay kinetics of $^{NCN}\mathbf{CN_x}$ (Figure S22). In the presence of 4-MBA, a more complete hole extraction was achieved in contrast to EDTA, as indicated by the lack of signal decay on sub-100 µs timescales. A small increase in the concentration of long-lived electrons was observed with 4-MBA, in line with the higher production of $H_2$ when using 4-MBA compared to EDTA.

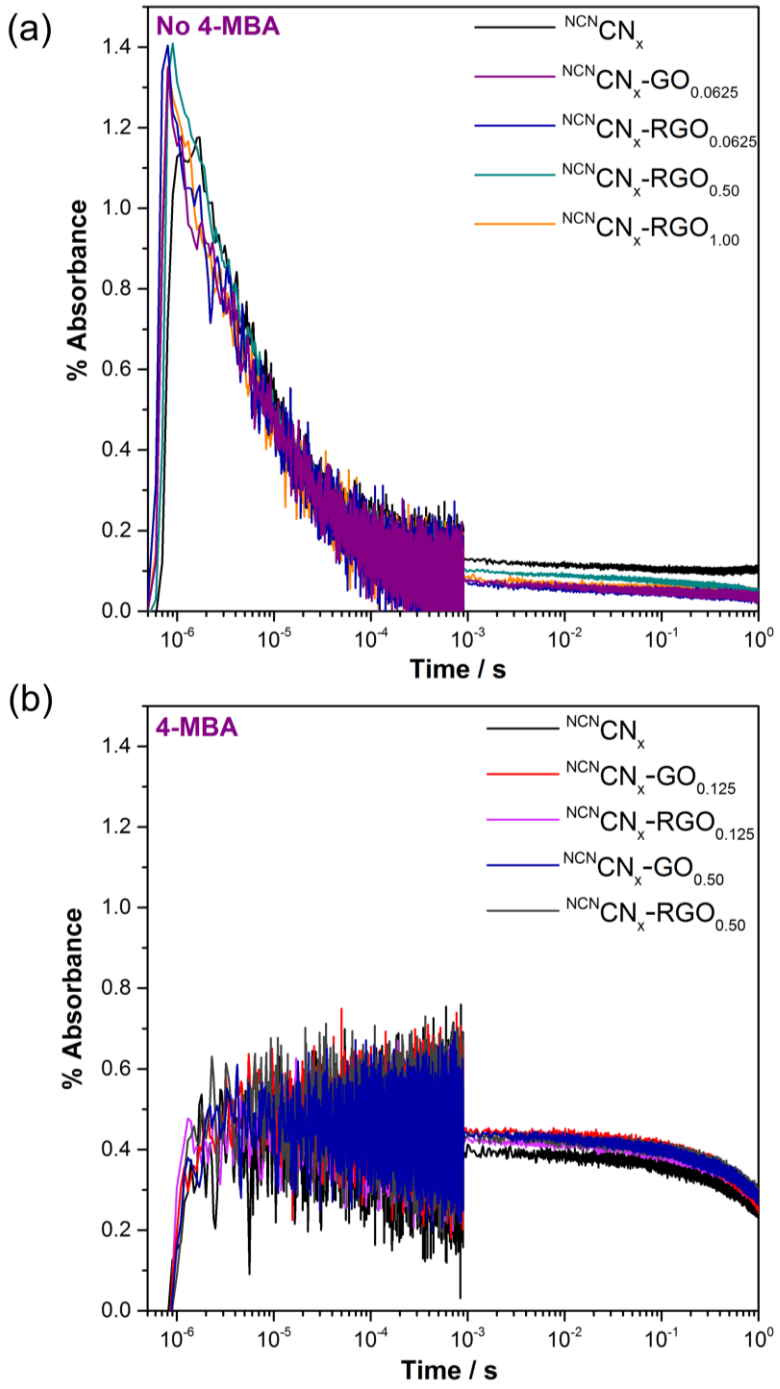


**Figure 4.** μs-TAS decay kinetics of (a) **$^{NCN}CN_x$** at the concentration of 1.67 mg $mL^{-1}$ dispersed in $KP_i$ solution (0.1 M, pH 4.5) with various GO and RGO loadings in the absence and (b) presence of 4-MBA (0.01 M), monitoring at $\lambda$ = 610 nm under $\lambda$ = 355 nm pulsed excitation.

**Decay kinetics of charged $^{NCN}CN_x$.** We next sought to investigate the electron transfer taking place from $^{NCN}CN_x$ to **NiP**, a vital step for $H_2$ production. This electron transfer has been shown to take place on a timescale longer than a few seconds.[35] During the measurements, $^{NCN}CN_x$ particles were settling in the cuvette, eliminating the possibility to accurately follow any process longer than 0.1 s and preventing an accurate measure of the electron transfer process. To overcome this issue of settling of $^{NCN}CN_x$, the powder was suspended in a non-intrusive matrix of a sodium deoxycholate (NaDC) hydrogel.[115] The matrix prevented the fast settling of $^{NCN}CN_x$, and the μs-TAS decay kinetics of aqueous $^{NCN}CN_x$ or $^{H_2N}CN_x$ suspensions and hydrogels were compared. The initial signal decay on the μs timescale was unchanged by the NaDC matrix (Figures S23 and S24) indicating that the $CN_x$ photophysics were not disrupted. The hydrogel matrix did successfully eliminate the artifacts caused by settling on timescales > 100 ms (Figure S23), particularly evident in the case of $^{H_2N}CN_x$.

Photoinduced absorption spectroscopy (PIAS) of hydrogel samples was then used to record the long-lived excited states and to monitor the electron transfer kinetics from $^{NCN}CN_x$ on the second to minute timescale. The samples were irradiated with a UV LED (365 nm, 0.5 mW $cm^{-2}$) pulse for 2 s, as opposed to the ns laser pulse used in TAS experiments. The change in absorbance was monitored at $\lambda$ = 610 nm during the LED excitation and 58 s following excitation. Similarly as for the TAS experiments, the signal detected is due to absorption from the photogenerated electrons, and the amplitude depends on the quantum yield of photogenerated electron, the recombination lifetime and the intensity of the excitation in steady-state conditions.[116]

PIAS traces were recorded for bare $^{NCN}$**CN$_x$** and hybrid systems with GO or RGO in the presence of different **NiP** concentrations (Figure S25). Similar traces were recorded for the different samples in the absence of **NiP**, pointing to insignificant changes in the $^{NCN}$**CN$_x$** photophysics when junctions with GO or RGO are introduced. In all cases, as the **NiP** concentration was increased, the absorbance signal was quenched faster, as expected: increasing the concentration of electron accepting molecules increases the rate of electron extraction. Interestingly, much faster absorption decays were observed by increasing the **NiP** concentration both in the presence of GO and RGO, as compared to bare $^{NCN}$**CN$_x$**. This trend was observed clearly when the normalized traces of $^{NCN}$**CN$_x$** and GO/RGO hybrids at a single **NiP** concentration are plotted together (Figure 5a and Figure S26). The data set of Figure 5a is also shown before normalization for comparison (Figure S27). The PIAS amplitude of all three types of samples after switching off the LED pulse for 10 s is also given (Figure 5b), again showing the stronger effect of the addition of **NiP** for the GO and RGO hybrids.

All the PIAS data clearly showed that the abstraction of the photoexcited electrons from $^{NCN}$**CN$_x$** is faster in the presence of GO and RGO. This qualitatively demonstrated that the interface between $^{NCN}$**CN$_x$** and GO or RGO enhanced the rate of electron extraction and delivery from $^{NCN}$**CN$_x$** to **NiP** on the second timescale. A quantitative description of the kinetics is prevented by the settling nature of the heterogeneous system, which is unfortunately not completely removed when using 13.8 mg mL$^{-1}$ NaDC to form the hydrogel matrix. We also note that addition of **NiP** and release of $Ni^{2+}$ ions may impact the viscoelastic properties of the hydrogels,[117,118] although this does not affect the comparison of the decay kinetics of different samples at the same **NiP** concentration. Stiffer matrices could be prepared

at higher NaDC concentrations to completely remove particle settling over the minute timescale, yet complete removal of oxygen, which has a strong impact on the observed kinetics (Figure S28) due to electron extraction, from the system was then prevented. This led to intractable variations between experiments and was not pursued further.

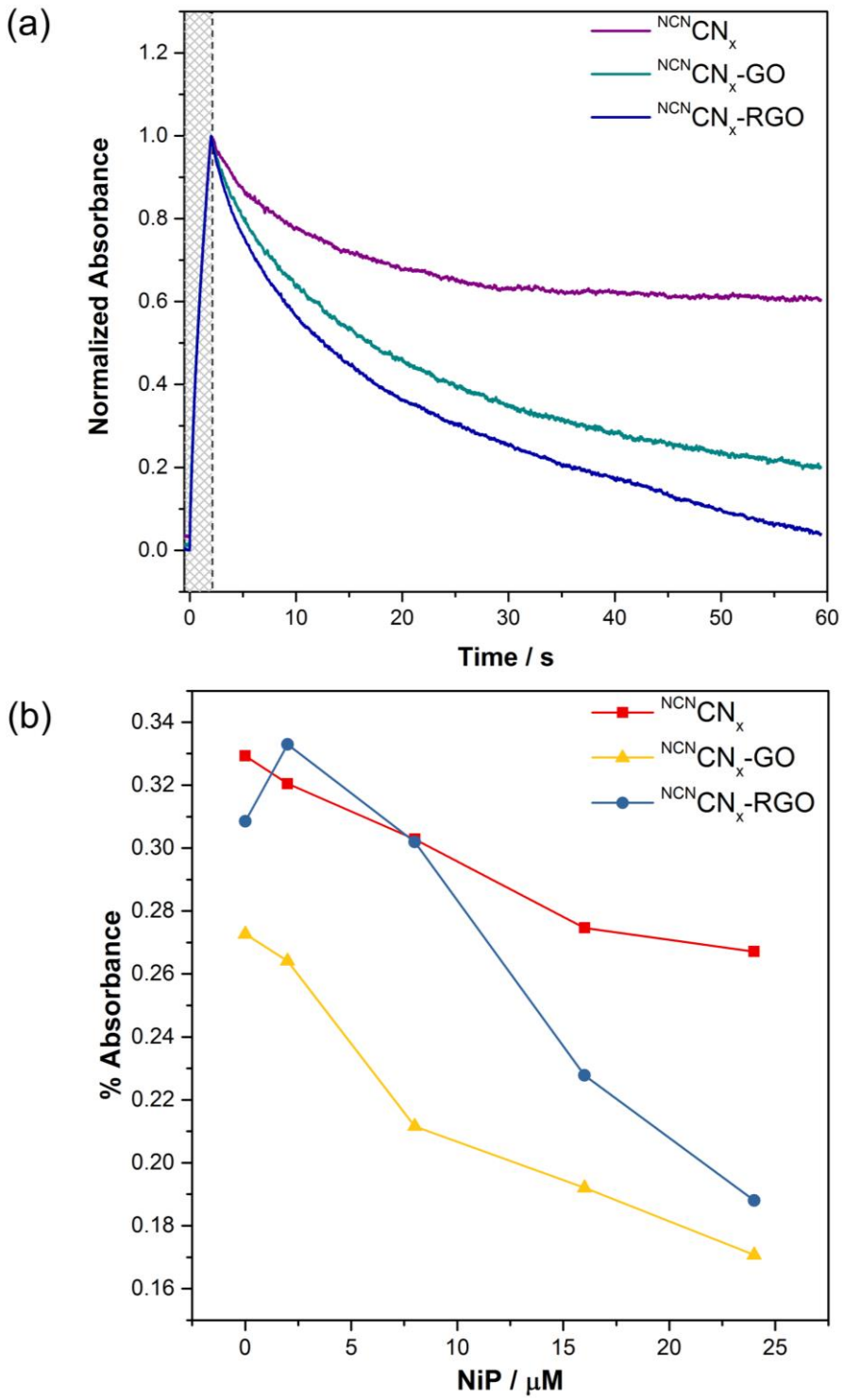


**Figure 5.** Comparison of PIAS of $^{NCN}$**CN$_x$**, $^{NCN}$**CN$_x$**-GO/RGO samples (0.125 wt% loading of GO or RGO, 6.3 μg) in NaDC (13.8 mg mL$^{-1}$) hydrogel monitored at $\lambda$ = 610 nm with LED excitation at $\lambda$ = 365 nm (0.5 mW cm$^{-2}$), in KP$_i$ solution (0.1 M, pH 4.5) with 4-MBA (0.01 M) under Ar (a) with **NiP** (24 μM) over 60 s and (b) at different **NiP** concentrations (10 seconds after switching off the light).

PIAS for bare $^{H_2N}CN_x$ and hybrids with GO/RGO were also conducted (Figure S29) and they all showed similar PIAS traces when considering both the amplitude and kinetics, even in the presence of **NiP**. While we expect to monitor only the unreactive trapped charges in the case of amino-terminated, $^{H_2N}CN_x$,[119] the lack of changes in the presence of GO and RGO supports our conclusion that the junction formed generally does not significantly impact the photophysics of $CN_x$.

Centrifugation experiments were subsequently conducted to better understand the interaction between GO and the **NiP** catalyst (Figure S30). First, the UV-visible absorption profile of **NiP** (50 nmol in 3 mL) was recorded alone in aqueous solution. Then, the **NiP** solution was stirred with different amounts of GO, specifically 0.05 mg and 0.5 mg. The resulting suspensions were then centrifuged (10,000 rpm, 10 min) and the UV-vis spectrum of **NiP** remaining in the supernatant was recorded. A significant reduction in the **NiP** absorption peaks was observed as the GO loading was increased, which can be attributed to H-bonding interactions between the -OH groups of GO or RGO and the phosphonate groups of the **NiP** catalyst.[120] This indicates that GO acts as a scaffold to bring **NiP** in close proximity to $^{NCN}CN_x$ and the greater affinity for the $^{NCN}CN_x$**-GO** interface enhances the rate of electron transfer from $^{NCN}CN_x$ to **NiP**. It was not possible to fully sediment $^{NCN}CN_x$ and RGO particles in analogous experiments, preventing us to clearly observe the absorption profile of **NiP**. Together, these observations highlight the importance of studying each component individually to develop better understanding on the charge generation and separation kinetics in multi component systems, by bringing photocatalytic experiments together with spectroscopic techniques.

## Conclusions

The enhanced activity of the closed photo-redox system $^{NCN}$**CN$_x$-NiP** is investigated upon integration with GO and RGO. Introducing GO/RGO enabled 3-times and 1.5-times enhancement in the presence of EDTA and 4-MBA, respectively. Systematic and precise tuning of the GO loading was found to be essential to reach the best photocatalytic performance due to the highly scattering nature of GO. A maximum specific activity of 4655 ± 448 µmol $H_2$ (g $^{NCN}CN_x)^{-1}$ $h^{-1}$ and a $TOF_{NiP}$ of 116 ± 3 $h^{-1}$ was reached through system optimization under 1 Sun irradiation. To the best of our knowledge, this is the highest activity reported in $CN_x$-GO/RGO heterojunction systems and top performance of "closed" $CN_x$ photocatalytic system for selective and stoichiometric alcohol oxidation and proton reduction. The catalytic activity of **NiP** is in line with previously reported colloidal systems. After 4 h of irradiation in the presence of GO, 18 ± 1 µmol of $H_2$ and 17 ± 1 µmol of 4-MBAd were obtained, corresponding to 57 ± 3 % of selective 4-MBA conversion.

Mechanistic investigations revealed that $^{NCN}$**CN$_x$** behaves as an electron reservoir for long-lived and reductive electrons, whereas the rate of electron extraction from $^{NCN}$**CN$_x$** is the overall limiting factor. The properties of the closed cycle were probed by optical spectroscopic techniques (PL, tr-PL, TAS, PIAS) to gain a better understanding on the charge transfer dynamics between $^{NCN}$**CN$_x$** and GO or RGO and **NiP**. In contrast to previous reports, our results revealed that introducing GO or RGO does not have a significant impact on charge separation or recombination on a timescale of < 0.1 s. The charge transfer reactions of the ultra-long-lived electrons in $^{NCN}$**CN$_x$** were probed by PIAS on timescales > 0.1 s. In the presence of GO and RGO, increasing **NiP** concentration resulted in faster quenching of the signal associated with the trapped electron in $^{NCN}$**CN$_x$** when compared with

bare $^{NCN}$**CN$_x$**. This effect indicates that GO and RGO improve the rate of electron extraction from $^{NCN}$**CN$_x$**. We show that **NiP** can interact with GO, which acts as a conductive binder and improves the affinity between **NiP** and $^{NCN}$**CN$_x$**. Therefore, the enhancement in activity upon addition of GO/RGO to $^{NCN}$**CN$_x$** and **NiP** is not a simple electronic effect but GO and RGO act as carbon scaffolds to efficiently bring the components in close proximity, without adversely affecting charge transport dynamics.

## Experimental Section.

**Materials.** All reagents used in synthesis were purchased from commercial suppliers and used directly without any further purification. The buffer solutions were prepared using analytical grade reagents and titrated to the desired pH with a pH meter (Mettler Toledo; SevenEasy).

***Synthesis of NiP and CN$_x$.*** **NiP** was synthesized and characterized as previously described.[75] $^{H_2N}$**CN$_x$** was prepared by a published procedure with a slight modification that the polymerization of the melamine was carried out at 550 °C for 4 h under air.[23,25] The yellow solid was thoroughly ground using a pestle and mortar prior to further analysis and applications. $^{NCN}$**CN$_x$** was prepared by grinding $^{H_2N}$**CN$_x$** and KSCN (weight ratio of 1:2; dried overnight at 140 °C under vacuum) and calcinating at 400 °C for 1h and then at 500 °C for 30 min under Ar as previously reported.[24] After cooling to room temperature the residual KSCN was removed by washing with water and the product was dried under vacuum at 60 °C.

***Preparation of GO and RGO.*** A modified Hummer's method was used to synthesize graphene oxide (GO).[121] In the preoxidation step, $H_2SO_4$ (20 mL) was slowly heated

up to 80 °C followed by the addition of $K_2S_2O_8$ (4.2 g) and $P_2O_5$ (4.2 g) with vigorous stirring. Graphite powder (5 g, Alfa Aesar, 325 mesh) was then added to the solution and the temperature was kept at 80 °C for 4.5 h followed by cooling down to room temperature. The mixture was diluted with water and left overnight. The mixture was repeatedly washed with deionized water (1 L) and centrifuged at 10,000 rpm followed by drying under air overnight to obtain a pre-oxidized product graphite oxide ($G_{ite}O$).

For the second oxidation step, $H_2SO_4$ (58 mL) was kept at 0 °C followed by the slow addition of $G_{ite}O$ (2.5 g) with vigorous stirring. Then, $KNO_3$ (1.25 g) and $KMnO_4$ (8 g) were slowly added while the temperature was kept below 10 °C. The mixture was then heated up to 35 °C and stirred for 2 h. After that, the mixture was diluted with water (58 mL) and stirred for 2 h, followed by addition of water (350 mL) to obtain a dark solution. $H_2O_2$ (25 mL 30%) was added dropwise to the solution and it was left overnight for stratification. The supernatant was decanted, and the gel sediment was washed with water and centrifuged with HCl for 5 times to remove the metal oxides. Then, the product was washed with water until the decantate was nearly neutral. Finally, the product was sonicated for 30 min and a dark brown GO gel was obtained. The GO gel was dried at 50 °C for 24 h. The reduction of GO to reduced graphene oxide (RGO) was carried out by adding 5 mg graphene oxide powder into a *L*-ascorbic acid solution (50 mL, 1 mg $mL^{-1}$) and vigorously stirring for 48 h, following a published procedure.[122]

**Characterization Techniques.** Fourier transform infrared spectra (FT-IR) of $^{NCN}CN_x$ were carried out on a Thermo Scientific Nicolet iS50 FT-IR spectrometer operating in an ATR mode. UV−visible spectroscopy was carried out on a Varian Cary 50 UV−vis

spectrophotometer using quartz cuvettes with 1 cm path length. The microscopic morphologies of $^{NCN}\mathbf{CN_x}$ samples were observed using a scanning electron microscope (SEM), Carl Zeiss CrossBeam, at an accelerating voltage of 10 kV. Raman spectra were obtained from a HORIBA LabRAM HR Evolution system with an incident laser of 532 nm. Transmission Electron Microscopy (TEM) were recorded with Tecnai G2 80-200kV transmission electron microscope.

Photoluminescence (PL) spectra of $^{NCN}\mathbf{CN_x}$ samples were recorded on an Edinburgh Instruments FS5 spectrofluorometer equipped with an integrating sphere. Emission scans were recorded with varying excitation wavelengths and the emission spectra were generated using a Fluoracle software provided with the FS5 instrument.

**Photocatalytic Experiments. $\mathbf{CN_x}$-GO/RGO** hybrids were prepared by stirring polymeric $^{NCN}\mathbf{CN_x}$ (5 mg) and different amounts of GO and RGO in a borosilicate glass photoreactor (total volume 7.74 mL) for 16 h prior to photocatalytic experiments. The amount of GO or RGO was specified by the weight percentage (wt%) of $\mathbf{CN_x}$, resulting in samples labelled as $GO_x$, in which x corresponds to weight percentage. An aqueous solution containing either EDTA or $KP_i$ buffer containing 4-MBA and **NiP** were added to the photoreactor with a stirrer bar (total volume 3 mL), which was then tightly sealed with a septum (Subaseal). The vials were then purged for at least 15 min with $N_2$ containing 2% $CH_4$, internal GC standard, before irradiation. The vials were then placed in a temperature-controlled water bath (25°C) with stirring and irradiated using a Xe lamp (Newport Oriel Solar Light Simulator, 100 mW $cm^{-2}$, 1 Sun). The set-up was equipped with an AM 1.5G filter and infrared irradiation was removed from all the experiments using a water filter.

**Quantification of Products.** The amount of $H_2$ was quantified using a GC (Agilent 7890A Series) equipped with a 5 Å molecular sieve column. The GC oven was kept at 45 °C and $N_2$ was used as the carrier gas. Approximately 20 µL of headspace gas was taken from the photoreactor for analysis periodically using an airtight Hamilton syringe.

The amounts of alcohol and aldehyde were quantified by nuclear magnetic resonance (NMR) spectroscopy. As the photoreactor was removed from irradiation the suspension was directly worked-up with 3 × $CH_2Cl_2$ (3 mL). The organic layers were then transferred into a round bottom flask and concentrated under reduced pressure. The residue was characterized by using $^1$H NMR spectroscopy on a Bruker DPX 400 *s*pectrometer at 25°C. The methyl peaks of the starting material and the product were used to determine the conversion yield.

The reliability of the work-up procedure was tested using different amounts of alcohol and aldehyde. The control experiments showed that the ratios were preserved after working up the solutions.

**Treatment of analytical data.** To ensure reproducibility, the solar light simulator and GC were calibrated regularly. All analytical measurements were carried out in triplicates and the data is reported as mean value ± standard deviation (σ). A minimum σ of 10% was assumed in all cases for photocatalytic experiments.

**Hydrogel Preparation.** Sodium deoxycholate (NaDC) powder was diluted in water at 13.8 mg mL$^{-1}$ concentration. This stock solution was then used to disperse $^{NCN}\mathbf{CN_x}$ or $^{H_2N}\mathbf{CN_x}$ powders and $KP_i$ buffer (1 M, pH 4.5) was added to prepare a final concentration of 0.1 M $KP_i$ and 1.67 mg mL$^{-1}$ of $\mathbf{CN_x}$. When 4-MBA was used in the experiments, it was previously added to the NaDC stock solution. The NaDC mixture with carbon nitrides ($^{NCN}\mathbf{CN_x}$ or $^{H_2N}\mathbf{CN_x}$) was heated up to ~ 60 °C for 15 min, then

$KP_i$ was added to the hot solution followed by an additional 15 min of heating. Afterwards, the mixture was left undisturbed and cooled down at room temperature to form the hydrogel.

**Steady-state-Spectroscopy.** A Shimadzu UV-2600 spectrometer equipped with an integrating sphere was used for recording UV-Vis diffuse reflectance spectra. Fluorescence spectra was recorded using a Jobin Yvon FluoroLog fluorometer. Steady-state spectra were acquired with powders dispersed in 1.67 mg $mL^{-1}$ in $KP_i$ (0.1 M, pH 4.5), under Ar, in 1 mm path length cuvettes.

**Time-correlated single photon counting (TCSPC).** The emissive states decay was monitored by TCSPC (DeltaFlex, Horiba). Data was acquired on two timescales (up to 100 ns and up to 6.5 µs) to follow the decay over several orders of magnitude. The various samples showed all the same initial intensities. Pulsed excitation of $\lambda$ = 404 nm (10 kHz repetition rate) was generated by a laser diode and fluorescence was detected at $\lambda$ = 490 nm (SPC-650 detector, Horiba). Excitation fluence was estimated to be ~ 20 $pJ/cm^2$. Both $^{NCN}\mathbf{CN_x}$ and $^{H_2N}\mathbf{CN_x}$ were dispersed in $KP_i$ at 1.67 mg $mL^{-1}$ and purged with Ar before acquisition.

**Transient Absorption Spectroscopy and Photoinduced Absorption Spectroscopy.** TAS decay on the ms–s timescale was acquired with the set up previously reported, in a diffuse reflectance mode.[35] The excitation source was a Nd:YAG laser (OPOTEK Opolette 355 II, 7 ns pulse width) that produced $\lambda$ = 355 nm light transmitted to the sample through a light guide. The excitation power density used is of 300 $\mu J/cm^2$. A 100 W Bentham IL1 quartz halogen lamp generated the probe light. Long pass filters (Comar Instruments) and an IR filter ($H_2O$, 5 cm path length) were positioned between the lamp and the sample to minimize short

wavelength irradiation and heating of the sample. The collection of diffuse reflectance from the sample was relayed to a monochromator (Oriel Cornerstone 130) through a long pass filter to select the probe wavelength. Acquisitions were triggered by a photodiode (Thorlabs DET10A) exposed to laser scatter. Time-resolved intensity data was collected with a Si photodiode (Hamamatsu S3071). For data at times faster than 1 ms, custom electronics (Costronics) amplified the electrical signal which was recorded by an oscilloscope (Tektronics DPO3012). Simultaneously, the data slower than 1 ms was recorded on a National Instrument DAQ card (NI USB-6251). Kinetic traces were typically obtained from the average of 32 laser pulses. Samples were prepared by dispersing $CN_x$ in $KP_i$ (0.1 M, pH 4.5) or in NaDC hydrogel to the concentration of 1.67 mg $mL^{-1}$, with or without 4-MBA and GO or RGO were added as required. The dispersion was transferred to 2 mm path length cuvettes. Samples in $KP_i$ were stirred prior to the start of each kinetic acquisition and were measured under Ar. Samples in hydrogel were degassed under Ar before all the acquisitions. Data was collected and processed using a home-built software written in the LabVIEW environment.

For the PIAS experiments, the monitoring wavelength was chosen as $\lambda$ = 610 and 800 nm for $^{NCN}\mathbf{CN_x}$ and $^{H_2N}\mathbf{CN_x}$ respectively in a diffuse reflectance mode. The samples prepared were irradiated with an LED at $\lambda$ = 365 nm (0.5 $mW.cm^{-2}$) for 2 seconds followed by 58 seconds off for $^{NCN}\mathbf{CN_x}$ and 5 s off for $^{H_2N}\mathbf{CN_x}$, and a single acquisition per wavelength per sample was performed.

## Associated Contents

Supporting tables and figures are included in the Supporting Information.

## Author Information


### Corresponding author

* reisner@ch.cam.ac.uk


### Notes

The authors declare no competing financial interest.

## Acknowledgements


This work was supported by the Christian Doppler Research Association (Austrian Federal Ministry of Science, Research, and Economy and the National Foundation for Research, Technology and Development), the OMV Group (to E.R.) and ERC AdG Intersolar (Grant 291482 to J.R.D.). We are grateful for the financial support from St Edmund's College (H.K.), FRQNT Postdoctoral Fellowship (R.G.) and from China Scholarship Council and Cambridge Trust (scholarship to X.F.). Dr. Heather F. Greer is greatly acknowledged for recording the TEM images. Dr. Souvik Roy, Mr. Constantin Sahm, Dr. Benjamin C. M. Martindale, Dr. Timothy E. Rosser, Dr. David Wakerley and Mr. Arjun Vijeta are acknowledged for their useful feedback and helpful discussions.


## Supporting Information

Supporting Information Available: Supporting Tables S1 to S10 and Supporting Figures S1 to S30. This material is available free of charge via the Internet at http://pubs.acs.org.

## References


(1) Ong, W.-J.; Tan, L.-L.; Ng, Y. H.; Yong, S.-T.; Chai, S.-P. Graphitic Carbon Nitride (g-$C_3N_4$)-Based Photocatalysts for Artificial Photosynthesis and Environmental Remediation: Are We a Step Closer To Achieving Sustainability? *Chem. Rev.* **2016**, *116*, 7159–7329.

(2) Quintana, M.; Edvinsson, T.; Hagfeldt, A.; Boschloo, G. Comparison of Dye-Sensitized ZnO and $TiO_2$ Solar Cells: Studies of Charge Transport and Carrier Lifetime. *J. Phys. Chem. C* **2007**, *111*, 1035–1041.

(3) Li, P.; Wei, Z.; Wu, T.; Peng, Q.; Li, Y. Au-ZnO hybrid nanopyramids and their photocatalytic properties. *J. Am. Chem. Soc.* **2011**, *133*, 5660–5663.

(4) Chen, X.; Burda, C. The Electronic Origin of the Visible-Light Absorption Properties of C-, N- and S-Doped $TiO_2$ Nanomaterials. *J. Am. Chem. Soc.* **2008**, *130*, 5018–5019.

(5) Chen, X.; Mao, S. S. Titanium dioxide nanomaterials: Synthesis, properties, modifications and applications. *Chem. Rev.* **2007**, *107*, 2891–2959.

(6) Warnan, J.; Willkomm, J.; Ng, J. N.; Godin, R.; Prantl, S.; Durrant, J. R.; Reisner, E. Solar $H_2$ evolution in water with modified diketopyrrolopyrrole dyes immobilised on molecular Co and Ni catalyst–$TiO_2$ hybrids. *Chem. Sci.* **2017**, *8*, 3070–3079.

(7) Kudo, A.; Miseki, Y. Heterogeneous photocatalyst materials for water splitting. *Chem. Soc. Rev.* **2009**, *38*, 253–278.

(8) Wakerley, D. W.; Kuehnel, M. F.; Orchard, K. L.; Ly, K. H.; Rosser, T. E.; Reisner, E. Solar-driven reforming of lignocellulose to $H_2$ with a $CdS/CdO_x$ photocatalyst. *Nat. Energy* **2017**, *2*, 17021.

(9) Han, Z.; Qiu, F.; Eisenberg, R.; Holland, P. L.; Krauss, T. D. Robust Photogeneration of $H_2$ in Water Using Semiconductor Nanocrystals and a Nickel Catalyst. *Science* **2012**, *338*, 1321–1324.

(10) Kuehnel, M. F.; Sahm, C. D.; Neri, G.; Lee, J. R.; Orchard, K. L.; Cowan, A. J.; Reisner, E. ZnSe quantum dots modified with a Ni(cyclam) catalyst for efficient visible-light driven $CO_2$ reduction in water. *Chem. Sci.* **2018**, *9*, 2501–2509.

(11) Martindale, B. C. M.; Hutton, G. A. M.; Caputo, C. A.; Reisner, E. Solar Hydrogen Production Using Carbon Quantum Dots and a Molecular Nickel Catalyst. *J. Am. Chem. Soc.* **2015**, *137*, 6018–6025.

(12) Martindale, B. C. M.; Hutton, G. A. M.; Caputo, C. A.; Prantl, S.; Godin, R.; Durrant, J. R.; Reisner, E. Enhancing Light Absorption and Charge Transfer Efficiency in Carbon Dots through Graphitization and Core Nitrogen Doping. *Angew. Chemie Int. Ed.* **2017**, *56*, 6459–6463.

(13) Yang, P.; Zhao, J.; Wang, J.; Cui, H.; Li, L.; Zhu, Z. Multifunctional Nitrogen-Doped Carbon Nanodots for Photoluminescence, Sensor, and Visible-Light-Induced $H_2$ Production. *ChemPhysChem* **2015**, *16*, 3058–3063.

(14) Hutton, G. A. M.; Martindale, B. C. M.; Reisner, E. Carbon dots as photosensitisers for solar-driven catalysis. *Chem. Soc. Rev.* **2017**, *46*, 6111–6123.

(15) Cao, S.; Low, J.; Yu, J.; Jaroniec, M. Polymeric Photocatalysts Based on Graphitic Carbon Nitride. *Adv. Mater.* **2015**, *27*, 2150–2176.

(16) Vilela, F.; Zhang, K.; Antonietti, M. Conjugated porous polymers for energy applications. *Energy Environ. Sci.* **2012**, *5*, 7819–7832.

(17) Gong, Y.; Li, M.; Wang, Y. Carbon Nitride in Energy Conversion and Storage: Recent Advances and Future Prospects. *ChemSusChem* **2015**, *8*, 931–946.

(18) Wang, X.; Maeda, K.; Thomas, A.; Takanabe, K.; Xin, G.; Carlsson, J. M.; Domen, K.; Antonietti, M. A metal-free polymeric photocatalyst for hydrogen production from water under visible light. *Nat. Mater.* **2009**, *8*, 76–80.

(19) Su, F.; Mathew, S. C.; Lipner, G.; Fu, X.; Antonietti, M.; Blechert, S.; Wang, X. mpg-$C_3N_4$-Catalyzed Selective Oxidation of Alcohols Using $O_2$ and Visible Light. *J. Am. Chem. Soc.* **2010**, *132*, 16299–16301.

(20) Cui, Y.; Ding, Z.; Liu, P.; Antonietti, M.; Fu, X.; Wang, X. Metal-free activation of $H_2O_2$ by g-$C_3N_4$ under visible light irradiation for the degradation of organic pollutants. *Phys. Chem. Chem. Phys.* **2012**, *14*, 1455–1462.

(21) Qiu, P.; Chen, H.; Xu, C.; Zhou, N.; Jiang, F.; Wang, X.; Fu, Y. Fabrication of an exfoliated graphitic carbon nitride as a highly active visible light photocatalyst. *J. Mater. Chem. A* **2015**, *3*, 24237–24244.

(22) Maeda, K.; Wang, X.; Nishihara, Y.; Lu, D.; Antonietti, M.; Domen, K. Photocatalytic Activities of Graphitic Carbon Nitride Powder for Water Reduction and Oxidation under Visible Light. *J. Phys. Chem. C* **2009**, *113*, 4940–4947.

(23) Caputo, C. A.; Gross, M. A.; Lau, V. W.-H.; Cavazza, C.; Lotsch, B. V.; Reisner, E. Photocatalytic Hydrogen Production using Polymeric Carbon

Nitride with a Hydrogenase and a Bioinspired Synthetic Ni Catalyst. *Angew. Chemie Int. Ed.* **2014**, *53*, 11538–11542.

(24) Lau, V. W.-H.; Moudrakovski, I.; Botari, T.; Weinberger, S.; Mesch, M. B.; Duppel, V.; Senker, J.; Blum, V.; Lotsch, B. V. Rational design of carbon nitride photocatalysts by identification of cyanamide defects as catalytically relevant sites. *Nat. Commun.* **2016**, *7*, 12165.

(25) Liu, J.; Liu, Y.; Liu, N.; Han, Y.; Zhang, X.; Huang, H.; Lifshitz, Y.; Lee, S.-T.; Zhong, J.; Kang, Z. Metal-free efficient photocatalyst for stable visible water splitting via a two-electron pathway. *Science* **2015**, *347*, 970–974.

(26) Zhu, M.; Kim, S.; Mao, L.; Fujitsuka, M.; Zhang, J.; Wang, X.; Majima, T. Metal-Free Photocatalyst for $H_2$ Evolution in Visible to Near-Infrared Region: Black Phosphorus/Graphitic Carbon Nitride. *J. Am. Chem. Soc.* **2017**, *139*, 13234–13242.

(27) Zhang, Y.; Mori, T.; Ye, J.; Antonietti, M. Phosphorus-Doped Carbon Nitride Solid: Enhanced Electrical Conductivity and Photocurrent Generation. *J. Am. Chem. Soc.* **2010**, *132*, 6294–6295.

(28) Wang, Y.; Li, H.; Yao, J.; Wang, X.; Antonietti, M. Synthesis of boron doped polymeric carbon nitride solids and their use as metal-free catalysts for aliphatic C–H bond oxidation. *Chem. Sci.* **2011**, *2*, 446–450.

(29) Li, J.; Shen, B.; Hong, Z.; Lin, B.; Gao, B.; Chen, Y. A facile approach to synthesize novel oxygen-doped g-$C_3N_4$ with superior visible-light photoreactivity. *Chem. Commun.* **2012**, *48*, 12017–12019.

(30) Ding, Z.; Chen, X.; Antonietti, M.; Wang, X. Synthesis of Transition Metal-Modified Carbon Nitride Polymers for Selective Hydrocarbon Oxidation.

*ChemSusChem* **2011**, *4*, 274–281.

(31) Gao, L.-F.; Wen, T.; Xu, J.-Y.; Zhai, X.-P.; Zhao, M.; Hu, G.-W.; Chen, P.; Wang, Q.; Zhang, H.-L. Iron-Doped Carbon Nitride-Type Polymers as Homogeneous Organocatalysts for Visible Light-Driven Hydrogen Evolution. *ACS Appl. Mater. Interfaces* **2016**, *8*, 617–624.

(32) Li, Z.; Kong, C.; Lu, G. Visible Photocatalytic Water Splitting and Photocatalytic Two-Electron Oxygen Formation over Cu- and Fe-Doped g-$C_3N_4$. *J. Phys. Chem. C* **2016**, *120*, 56–63.

(33) Yang, S.; Gong, Y.; Zhang, J.; Zhan, L.; Ma, L.; Fang, Z.; Vajtai, R.; Wang, X.; Ajayan, P. M. Exfoliated graphitic carbon nitride nanosheets as efficient catalysts for hydrogen evolution under visible light. *Adv. Mater.* **2013**, *25*, 2452–2456.

(34) Zhan, Y.; Liu, Z.; Liu, Q.; Huang, D.; Wei, Y.; Hu, Y.; Lian, X.; Hu, C. A facile and one-pot synthesis of fluorescent graphitic carbon nitride quantum dots for bio-imaging applications. *New J. Chem.* **2017**, *41*, 3930–3938.

(35) Kasap, H.; Caputo, C. A.; Martindale, B. C. M.; Godin, R.; Lau, V. W.-H.; Lotsch, B. V.; Durrant, J. R.; Reisner, E. Solar-Driven Reduction of Aqueous Protons Coupled to Selective Alcohol Oxidation with a Carbon Nitride–Molecular Ni Catalyst System. *J. Am. Chem. Soc.* **2016**, *138*, 9183–9192.

(36) Allen, M. J.; Tung, V. C.; Kaner, R. B. Honeycomb carbon: A review of graphene. *Chem. Rev.* **2010**, *110*, 132–145.

(37) Geim, A. K.; Novoselov, K. S. The rise of graphene. *Nat. Mater.* **2007**, *6*, 183–191.

(38) Xiang, Q.; Yu, J.; Jaroniec, M. Graphene-based semiconductor photocatalysts.

*Chem. Soc. Rev.* **2012**, *41*, 782–796.

(39) Yang, M.-Q.; Xu, Y.-J. Selective photoredox using graphene-based composite photocatalysts. *Phys. Chem. Chem. Phys.* **2013**, *15*, 19102–19118.

(40) Novoselov, K. S.; Geim, A. K.; Morozov, S. V; Jiang, D.; Zhang, Y.; Dubonos, S. V; Grigorieva, I. V; Firsov, A. A. Electric field effect in atomically thin carbon films. *Science* **2004**, *306*, 666–669.

(41) Luo, J.; Cote, L. J.; Tung, V. C.; Tan, A. T. L.; Goins, P. E.; Wu, J.; Huang, J. Graphene oxide nanocolloids. *J. Am. Chem. Soc.* **2010**, *132*, 17667–17669.

(42) Luo, J.; Kim, J.; Huang, J. Material processing of chemically modified graphene: Some challenges and solutions. *Acc. Chem. Res.* **2013**, *46*, 2225–2234.

(43) Sun, Y.; Wu, Q.; Shi, G. Graphene based new energy materials. *Energy Environ. Sci.* **2011**, *4*, 1113–1132.

(44) Ng, Y. H.; Iwase, A.; Kudo, A.; Amal, R. Reducing graphene oxide on a visible-light $BiVO_4$ photocatalyst for an enhanced photoelectrochemical water splitting. *J. Phys. Chem. Lett.* **2010**, *1*, 2607–2612.

(45) Iwase, A.; Ng, Y. H.; Ishiguro, Y.; Kudo, A.; Amal, R. Reduced Graphene Oxide as a Solid-State Electron Mediator in Z-Scheme Photocatalytic Water Splitting under Visible Light. *J. Am. Chem. Soc.* **2011**, *133*, 11054–11057.

(46) Xiang, Q.; Yu, J.; Jaroniec, M. Enhanced photocatalytic $H_2$-production activity of graphene-modified titania nanosheets. *Nanoscale* **2011**, *3*, 3670–3678.

(47) Xiang, Q.; Yu, J.; Jaroniec, M. Preparation and Enhanced Visible-Light Photocatalytic $H_2$-Production Activity of Graphene/$C_3N_4$ Composites. *J. Phys.*

*Chem. C* **2011**, *115*, 7355–7363.

(48) Min, S.; Lu, G. Dye-sensitized reduced graphene oxide photocatalysts for highly efficient visible-light-driven water reduction. *J. Phys. Chem. C* **2011**, *115*, 13938–13945.

(49) Tu, W.; Zhou, Y.; Liu, Q.; Yan, S.; Bao, S.; Wang, X.; Xiao, M.; Zou, Z. An In Situ Simultaneous Reduction-Hydrolysis Technique for Fabrication of $TiO_2$-Graphene 2D Sandwich-Like Hybrid Nanosheets: Graphene-Promoted Selectivity of Photocatalytic-Driven Hydrogenation and Coupling of $CO_2$ into Methane and Eth. *Adv. Funct. Mater.* **2013**, *23*, 1743–1749.

(50) Yu, J.; Jin, J.; Cheng, B.; Jaroniec, M. A noble metal-free reduced graphene oxide–CdS nanorod composite for the enhanced visible-light photocatalytic reduction of $CO_2$ to solar fuel. *J. Mater. Chem. A* **2014**, *2*, 3407–3416.

(51) Shown, I.; Hsu, H.-C.; Chang, Y.-C.; Lin, C.-H.; Roy, P. K.; Ganguly, A.; Wang, C.-H.; Chang, J.-K.; Wu, C.-I.; Chen, L.-C.; Chen, K.-H. Highly Efficient Visible Light Photocatalytic Reduction of $CO_2$ to Hydrocarbon Fuels by Cu-Nanoparticle Decorated Graphene Oxide. *Nano Lett.* **2014**, *14*, 6097–6103.

(52) Xu, Y.-F.; Yang, M.-Z.; Chen, B.-X.; Wang, X.-D.; Chen, H.-Y.; Kuang, D.-B.; Su, C.-Y. A $CsPbBr_3$ Perovskite Quantum Dot/Graphene Oxide Composite for Photocatalytic $CO_2$ Reduction. *J. Am. Chem. Soc.* **2017**, *139*, 5660–5663.

(53) Iwashina, K.; Iwase, A.; Ng, Y. H.; Amal, R.; Kudo, A. Z-schematic water splitting into $H_2$ and $O_2$ using metal sulfide as a hydrogen-evolving photocatalyst and reduced graphene oxide as a solid-state electron mediator. *J. Am. Chem. Soc.* **2015**, *137*, 604–607.

(54) Pan, Z.; Hisatomi, T.; Wang, Q.; Chen, S.; Iwase, A.; Nakabayashi, M.;

Shibata, N.; Takata, T.; Katayama, M.; Minegishi, T.; Kudo, A.; Domen, K. Photoreduced Graphene Oxide as a Conductive Binder to Improve the Water Splitting Activity of Photocatalyst Sheets. *Adv. Funct. Mater.* **2016**, *26*, 7011–7019.

(55) Mateo, D.; Esteve-Adell, I.; Albero, J.; Royo, J. F. S.; Primo, A.; Garcia, H. 111 oriented gold nanoplatelets on multilayer graphene as visible light photocatalyst for overall water splitting. *Nat. Commun.* **2016**, *7*, 11819.

(56) Iwase, A.; Yoshino, S.; Takayama, T.; Ng, Y. H.; Amal, R.; Kudo, A. Water Splitting and $CO_2$ Reduction under Visible Light Irradiation Using Z-Scheme Systems Consisting of Metal Sulfides, CoOx-Loaded $BiVO_4$, and a Reduced Graphene Oxide Electron Mediator. *J. Am. Chem. Soc.* **2016**, *138*, 10260–10264.

(57) Zhang, Y.; Tang, Z.-R.; Fu, X.; Xu, Y.-J. Engineering the Unique 2D Mat of Graphene to Achieve Graphene-$TiO_2$ Nanocomposite for Photocatalytic Selective Transformation: What Advantage does Graphene Have over Its Forebear Carbon Nanotube? *ACS Nano* **2011**, *5*, 7426–7435.

(58) Zhang, N.; Yang, M.-Q.; Tang, Z.-R.; Xu, Y.-J. CdS–graphene nanocomposites as visible light photocatalyst for redox reactions in water: A green route for selective transformation and environmental remediation. *J. Catal.* **2013**, *303*, 60–69.

(59) Liu, S.; Chen, Z.; Zhang, N.; Tang, Z.-R.; Xu, Y.-J. An Efficient Self-Assembly of CdS Nanowires–Reduced Graphene Oxide Nanocomposites for Selective Reduction of Nitro Organics under Visible Light Irradiation. *J. Phys. Chem. C* **2013**, *117*, 8251–8261.

(60) Zhang, N.; Zhang, Y.; Pan, X.; Yang, M.-Q.; Xu, Y.-J. Constructing Ternary CdS–Graphene–$TiO_2$ Hybrids on the Flatland of Graphene Oxide with Enhanced Visible-Light Photoactivity for Selective Transformation. *J. Phys. Chem. C* **2012**, *116*, 18023–18031.

(61) Zhang, H.; Lv, X.; Li, Y.; Wang, Y.; Li, J. P25-Graphene Composite as a High Performance Photocatalyst. *ACS Nano* **2010**, *4*, 380–386.

(62) Zhang, Y.; Tang, Z.-R.; Fu, X.; Xu, Y.-J. $TiO_2$−Graphene Nanocomposites for Gas-Phase Photocatalytic Degradation of Volatile Aromatic Pollutant: Is $TiO_2$−Graphene Truly Different from Other $TiO_2$−Carbon Composite Materials? *ACS Nano* **2010**, *4*, 7303–7314.

(63) Xiang, Q.; Lang, D.; Shen, T.; Liu, F. Graphene-modified nanosized $Ag_3PO_4$ photocatalysts for enhanced vsible-light photocatalytic activity and stability. *Appl. Catal. B Environ.* **2015**, *162*, 196–203.

(64) Lou, J.; Liu, Y.; Wang, Z.; Zhao, D.; Song, C.; Wu, J.; Dasgupta, N.; Zhang, W.; Zhang, D.; Tao, P.; Shang, W.; Deng, T. Bioinspired Multifunctional Paper-Based rGO Composites for Solar-Driven Clean Water Generation. *ACS Appl. Mater. Interfaces* **2016**, *8*, 14628–14636.

(65) Xiang, Q.; Cheng, B.; Yu, J. Graphene-Based Photocatalysts for Solar-Fuel Generation. *Angew. Chemie Int. Ed.* **2015**, *54*, 11350–11366.

(66) Liu, Z.; Liu, Q.; Huang, Y.; Ma, Y.; Yin, S.; Zhang, X.; Sun, W.; Chen, Y. Organic photovoltaic devices based on a novel acceptor material: Graphene. *Adv. Mater.* **2008**, *20*, 3924–3930.

(67) Li, S.-S.; Tu, K.-H.; Lin, C.-C.; Chen, C.-W.; Chhowalla, M. Solution-Processable Graphene Oxide as an Efficient Hole Transport Layer in Polymer

Solar Cells. *ACS Nano* **2010**, *4*, 3169–3174.

(68) Liu, J.; Durstock, M.; Dai, L. Graphene oxide derivatives as hole- and electron-extraction layers for high-performance polymer solar cells. *Energy Environ. Sci.* **2014**, *7*, 1297–1306.

(69) Lee, D.-Y.; Na, S.-I.; Kim, S.-S. Graphene oxide/PEDOT:PSS composite hole transport layer for efficient and stable planar heterojunction perovskite solar cells. *Nanoscale* **2016**, *8*, 1513–1522.

(70) Liu, Q.; Liu, Z.; Zhang, X.; Yang, L.; Zhang, N.; Pan, G.; Yin, S.; Chen, Y.; Wei, J. Polymer Photovoltaic Cells Based on Solution-Processable Graphene and P3HT. *Adv. Funct. Mater.* **2009**, *19*, 894–904.

(71) Yu, D.; Park, K.; Durstock, M.; Dai, L. Fullerene-grafted graphene for efficient bulk heterojunction polymer photovoltaic devices. *J. Phys. Chem. Lett.* **2011**, *2*, 1113–1118.

(72) Wang, D. H.; Kim, J. K.; Seo, J. H.; Park, I.; Hong, B. H.; Park, J. H.; Heeger, A. J. Transferable graphene oxide by stamping nanotechnology: Electron-transport layer for efficient bulk-heterojunction solar cells. *Angew. Chemie - Int. Ed.* **2013**, *52*, 2874–2880.

(73) Helm, M. L.; Stewart, M. P.; Bullock, R. M.; DuBois, M. R.; DuBois, D. L. A Synthetic Nickel Electrocatalyst with a Turnover Frequency Above 100,000 $s^{-1}$ for $H_2$ Production. *Science* **2011**, *333*, 863–866.

(74) Kilgore, U. J.; Roberts, J. A. S.; Pool, D. H.; Appel, A. M.; Stewart, M. P.; DuBois, M. R.; Dougherty, W. G.; Kassel, W. S.; Bullock, R. M.; DuBois, D. L. $[Ni(P^{Ph}_2N^{C6H4X}_2)_2]^{2+}$ Complexes as Electrocatalysts for $H_2$ Production: Effect of Substituents, Acids, and Water on Catalytic Rates. *J. Am. Chem. Soc.* **2011**,

*133*, 5861–5872.

(75) Gross, M. A.; Reynal, A.; Durrant, J. R.; Reisner, E. Versatile Photocatalytic Systems for $H_2$ Generation in Water Based on an Efficient DuBois-Type Nickel Catalyst. *J. Am. Chem. Soc.* **2014**, *136*, 356–366.

(76) Creissen, C. E.; Warnan, J.; Reisner, E. Solar $H_2$ generation in water with a $CuCrO_2$ photocathode modified with an organic dye and molecular Ni catalyst. *Chem. Sci.* **2018**, *9*, 1439–1447.

(77) Leung, J. J.; Warnan, J.; Nam, D. H.; Zhang, J. Z.; Willkomm, J.; Reisner, E. Photoelectrocatalytic $H_2$ evolution in water with molecular catalysts immobilised on p-Si via a stabilising mesoporous $TiO_2$ interlayer. *Chem. Sci.* **2017**, *8*, 5172–5180.

(78) Horvath-Bordon, E.; Kroke, E.; Svoboda, I.; Fuess, H.; Riedel, R. Potassium melonate, $K_3[C_6N_7(NCN)_3]\cdot 5H_2O$, and its potential use for the synthesis of graphite-like $C_3N_4$ materials. *New J. Chem.* **2005**, *29*, 693–699.

(79) Wang, T.; Li, C.; Ji, J.; Wei, Y.; Zhang, P.; Wang, S.; Fan, X.; Gong, J. Reduced Graphene Oxide (rGO)/$BiVO_4$ Composites with Maximized Interfacial Coupling for Visible Lght Photocatalysis. *ACS Sustain. Chem. Eng.* **2014**, *2*, 2253–2258.

(80) Liao, G.; Chen, S.; Quan, X.; Yu, H.; Zhao, H. Graphene oxide modified g-$C_3N_4$ hybrid with enhanced photocatalytic capability under visible light irradiation. *J. Mater. Chem.* **2012**, *22*, 2721–2726.

(81) Yeh, T.-F.; Teng, C.-Y.; Chen, S.-J.; Teng, H. Nitrogen-Doped Graphene Oxide Quantum Dots as Photocatalysts for Overall Water-Splitting under Visible Light Illumination. *Adv. Mater.* **2014**, *26*, 3297–3303.

(82) Yeh, T.-F.; Syu, J.-M.; Cheng, C.; Chang, T.-H.; Teng, H. Graphite Oxide as a Photocatalyst for Hydrogen Production from Water. *Adv. Funct. Mater.* **2010**, *20*, 2255–2262.

(83) Yeh, T.-F.; Chan, F.-F.; Hsieh, C.-T.; Teng, H. Graphite Oxide with Different Oxygenated Levels for Hydrogen and Oxygen Production from Water under Illumination: The Band Positions of Graphite Oxide. *J. Phys. Chem. C* **2011**, *115*, 22587–22597.

(84) Li, K.; Xie, X.; Zhang, W.-D. Porous Graphitic Carbon Nitride Derived from Melamine-Ammonium Oxalate Stacking Sheets with Excellent Photocatalytic Hydrogen Evolution Activity. *ChemCatChem* **2016**, *8*, 2128–2135.

(85) Wang, H.; Wang, B.; Bian, Y.; Dai, L. Enhancing Photocatalytic Activity of Graphitic Carbon Nitride by Codoping with P and C for Efficient Hydrogen Generation. *ACS Appl. Mater. Interfaces* **2017**, *9*, 21730–21737.

(86) Qin, J.; Huo, J.; Zhang, P.; Zeng, J.; Wang, T.; Zeng, H. Improving the photocatalytic hydrogen production of Ag/g-$C_3N_4$ nanocomposites by dye-sensitization under visible light irradiation. *Nanoscale* **2016**, *8*, 2249–2259.

(87) Song, L.; Li, T.; Zhang, S. Fullerenes/Graphite Carbon Nitride with Enhanced Photocatalytic Hydrogen Evolution Ability. *J. Phys. Chem. C* **2017**, *121*, 293–299.

(88) Martin, D. J.; Qiu, K.; Shevlin, S. A.; Handoko, A. D.; Chen, X.; Guo, Z.; Tang, J. Highly Efficient Photocatalytic $H_2$ Evolution from Water using Visible Light and Structure-Controlled Graphitic Carbon Nitride. *Angew. Chemie Int. Ed.* **2014**, *53*, 9240–9245.

(89) Li, X.; Shen, R.; Ma, S.; Chen, X.; Xie, J. Graphene-based heterojunction

photocatalysts. *Appl. Surf. Sci.* **2018**, *430*, 53–107.

(90) Wang, P.; Guan, Z.; Li, Q.; Yang, J. Efficient visible-light-driven photocatalytic hydrogen production from water by using Eosin Y-sensitized novel g-$C_3N_4$/Pt/GO composites. *J. Mater. Sci.* **2018**, *53*, 774–786.

(91) Zeng, P.; Zhang, Q.; Peng, T.; Zhang, X. One-pot synthesis of reduced graphene oxide-cadmium sulfide nanocomposite and its photocatalytic hydrogen production. *Phys. Chem. Chem. Phys.* **2011**, *13*, 21496–21502.

(92) Li, Q.; Guo, B.; Yu, J.; Ran, J.; Zhang, B.; Yan, H.; Gong, J. R. Highly Efficient Visible-Light-Driven Photocatalytic Hydrogen Production of CdS-Cluster-Decorated Graphene Nanosheets. *J. Am. Chem. Soc.* **2011**, *133*, 10878–10884.

(93) Lau, V. W.-H.; Klose, D.; Kasap, H.; Podjaski, F.; Pignié, M.-C.; Reisner, E.; Jeschke, G.; Lotsch, B. V. Dark Photocatalysis: Storage of Solar Energy in Carbon Nitride for Time-Delayed Hydrogen Generation. *Angew. Chemie Int. Ed.* **2017**, *56*, 510–514.

(94) Su, F.; Mathew, S. C.; Möhlmann, L.; Antonietti, M.; Wang, X.; Blechert, S. Aerobic Oxidative Coupling of Amines by Carbon Nitride Photocatalysis with Visible Light. *Angew. Chemie Int. Ed.* **2011**, *50*, 657–660.

(95) Long, B.; Ding, Z.; Wang, X. Carbon Nitride for the Selective Oxidation of Aromatic Alcohols in Water under Visible Light. *ChemSusChem* **2013**, *6*, 2074–2078.

(96) Higashimoto, S.; Suetsugu, N.; Azuma, M.; Ohue, H.; Sakata, Y. Efficient and selective oxidation of benzylic alcohol by $O_2$ into corresponding aldehydes on a $TiO_2$ photocatalyst under visible light irradiation: Effect of phenyl-ring

substitution on the photocatalytic activity. *J. Catal.* **2010**, *274*, 76–83.

(97) Shi, T.; Chang, W.; Zhang, H.; Ji, H.; Ma, W.; Chen, C.; Zhao, J. $H_2O$-Involved Two-Electron Pathway for Photooxidation of Aldehydes on $TiO_2$: An Isotope Labeling Study. *Environ. Sci. Technol.* **2015**, *49*, 3024–3031.

(98) Zhao, L.; Zhang, B.; Xiao, X.; Gu, F. L.; Zhang, R.-Q. Roles of the active species involved in the photocatalytic oxidation of benzyl alcohol into benzaldehyde on $TiO_2$ under UV light: Experimental and DFT studies. *J. Mol. Catal. A Chem.* **2016**, *420*, 82–87.

(99) Yuan, B.; Chong, R.; Zhang, B.; Li, J.; Liu, Y.; Li, C. Photocatalytic aerobic oxidation of amines to imines on $BiVO_4$ under visible light irradiation. *Chem. Commun.* **2014**, *50*, 15593–15596.

(100) Zhang, B.; Li, J.; Zhang, B.; Chong, R.; Li, R.; Yuan, B.; Lu, S.-M.; Li, C. Selective oxidation of sulfides on Pt/$BiVO_4$ photocatalyst under visible light irradiation using water as the oxygen source and dioxygen as the electron acceptor. *J. Catal.* **2015**, *332*, 95–100.

(101) Ahmed, A. Y.; Kandiel, T. A.; Ivanova, I.; Bahnemann, D. Photocatalytic and photoelectrochemical oxidation mechanisms of methanol on $TiO_2$ in aqueous solution. *Appl. Surf. Sci.* **2014**, *319*, 44–49.

(102) Wang, F.; Jiang, Y.; Gautam, A.; Li, Y.; Amal, R. Exploring the Origin of Enhanced Activity and Reaction Pathway for Photocatalytic $H_2$ Production on Au/B-$TiO_2$ Catalysts. *ACS Catal.* **2014**, *4*, 1451–1457.

(103) Zhao, L.-M.; Meng, Q.-Y.; Fan, X.-B.; Ye, C.; Li, X.-B.; Chen, B.; Ramamurthy, V.; Tung, C.-H.; Wu, L.-Z. Photocatalysis with Quantum Dots and Visible Light: Selective and Efficient Oxidation of Alcohols to Carbonyl Compounds through

a Radical Relay Process in Water. *Angew. Chem. Int. Ed. Engl.* **2017**, *56*, 3020–3024.

(104) Westheimer, F. H. The Magnitude of the Primary Kinetic Isotope Effect for Compounds of Hydrogen and Deuterium. *Chem. Rev.* **1961**, *61*, 265–273.

(105) Roecker, L.; Meyer, T. J. Hydride Transfer in the Oxidation of Alcohols by $[(bpy)_2(py)Ru(O)]^{2+}$. A kH/kD Kinetic Isotope Effect of 50. *J. Am. Chem. Soc.* **1987**, *109*, 746–754.

(106) Morimoto, Y.; Park, J.; Suenobu, T.; Lee, Y.-M.; Nam, W.; Fukuzumi, S. Mechanistic Borderline of One-Step Hydrogen Atom Transfer versus Stepwise $Sc^{3+}$-Coupled Electron Transfer from Benzyl Alcohol Derivatives to a Non-Heme Iron(IV)-Oxo Complex. *Inorg. Chem.* **2012**, *51*, 10025–10036.

(107) Li, H.; Liu, R.; Lian, S.; Liu, Y.; Huang, H.; Kang, Z. Near-infrared light controlled photocatalytic activity of carbon quantum dots for highly selective oxidation reaction. *Nanoscale* **2013**, *5*, 3289–3297.

(108) Zhang, J.; Chen, X.; Takanabe, K.; Maeda, K.; Domen, K.; Epping, J. D.; Fu, X.; Antonietti, M.; Wang, X. Synthesis of a Carbon Nitride Structure for Visible-Light Catalysis by Copolymerization. *Angew. Chemie Int. Ed.* **2010**, *49*, 441–444.

(109) Megerle, U.; Wenninger, M.; Kutta, R.-J.; Lechner, R.; König, B.; Dick, B.; Riedle, E. Unraveling the flavin-catalyzed photooxidation of benzylic alcohol with transient absorption spectroscopy from sub-pico- to microseconds. *Phys. Chem. Chem. Phys.* **2011**, *13*, 8869–8880.

(110) Kongkanand, A.; Kamat, P. V. Electron Storage in Single Wall Carbon Nanotubes. Fermi Level Equilibration in Semiconductor–SWCNT Suspensions.

*ACS Nano* **2007**, *1*, 13–21.

(111) Nelson, J. Diffusion-limited recombination in polymer-fullerene blends and its influence on photocurrent collection. *Phys. Rev. B* **2003**, *67*, 155209.

(112) Barzykin, A. V; Tachiya, M. Mechanism of Charge Recombination in Dye-Sensitized Nanocrystalline Semiconductors:Random Flight Model. *J. Phys. Chem. A* **2002**, *106*, 4356–4363.

(113) Lightcap, I. V.; Kamat, P. V. Fortification of CdSe Quantum Dots with Graphene Oxide. Excited State Interactions and Light Energy Conversion. *J. Am. Chem. Soc.* **2012**, *134*, 7109–7116.

(114) Rahman, M. Z.; Zhang, J.; Tang, Y.; Davey, K.; Qiao, S.-Z. Graphene oxide coupled carbon nitride homo-heterojunction photocatalyst for enhanced hydrogen production. *Mater. Chem. Front.* **2017**, *1*, 562–571.

(115) Liang, W.; Guman-Sepulveda, J. R.; He, S.; Dogariu, A.; Fang, J. Y. Microrheology and Release Behaviors of Self-Assembled Steroid Hydrogels. *J. Mater. Sci. Chem. Eng.* **2015**, *3*, 6–15.

(116) Boschloo, G.; Hagfeldt, A. Photoinduced absorption spectroscopy as a tool in the study of dye-sensitized solar cells. *Inorganica Chim. Acta* **2008**, *361*, 729–734.

(117) Chakrabarty, A.; Maitra, U.; Das, A. D. Metal cholate hydrogels: versatile supramolecular systems for nanoparticle embedded soft hybrid materials. *J. Mater. Chem.* **2012**, *22*, 18268–18278.

(118) Zhang, J.; Wang, H.; Li, X.; Song, S.; Song, A.; Hao, J. Two Gelation Mechanisms of Deoxycholate with Inorganic Additives: Hydrogen Bonding and Electrostatic Interactions. *J. Phys. Chem. B* **2016**, *120*, 6812–6818.

(119) Godin, R.; Wang, Y.; Zwijnenburg, M. A.; Tang, J.; Durrant, J. R. Time-Resolved Spectroscopic Investigation of Charge Trapping in Carbon Nitrides Photocatalysts for Hydrogen Generation. *J. Am. Chem. Soc.* **2017**, *139*, 5216–5224.

(120) Ye, S.; Ding, C.; Chen, R.; Fan, F.; Fu, P.; Yin, H.; Wang, X.; Wang, Z.; Du, P.; Li, C. Mimicking the Key Functions of Photosystem II in Artificial Photosynthesis for Photoelectrocatalytic Water Splitting. *J. Am. Chem. Soc.* **2018**, *140*, 3250–3256.

(121) Sun, H.; You, X.; Deng, J.; Chen, X.; Yang, Z.; Ren, J.; Peng, H. Novel graphene/carbon nanotube composite fibers for efficient wire-shaped miniature energy devices. *Adv. Mater.* **2014**, *26*, 2868–2873.

(122) Zhang, J.; Yang, H.; Shen, G.; Cheng, P.; Zhang, J.; Guo, S. Reduction of graphene oxide via L-ascorbic acid. *Chem. Commun.* **2010**, *46*, 1112–1114.

## Table of Contents